



저작자표시-비영리-변경금지 2.0 대한민국

이용자는 아래의 조건을 따르는 경우에 한하여 자유롭게

- 이 저작물을 복제, 배포, 전송, 전시, 공연 및 방송할 수 있습니다.

다음과 같은 조건을 따라야 합니다:



저작자표시. 귀하는 원저작자를 표시하여야 합니다.



비영리. 귀하는 이 저작물을 영리 목적으로 이용할 수 없습니다.



변경금지. 귀하는 이 저작물을 개작, 변형 또는 가공할 수 없습니다.

- 귀하는, 이 저작물의 재이용이나 배포의 경우, 이 저작물에 적용된 이용허락조건을 명확하게 나타내어야 합니다.
- 저작권자로부터 별도의 허가를 받으면 이러한 조건들은 적용되지 않습니다.

저작권법에 따른 이용자의 권리는 위의 내용에 의하여 영향을 받지 않습니다.

이것은 [이용허락규약\(Legal Code\)](#)을 이해하기 쉽게 요약한 것입니다.

[Disclaimer](#)

공학박사 학위논문

Plasma resistant coating using  
suspension plasma spraying and  
aerosol deposition

서스펜션 플라즈마 스프레이와 에어로졸 증착  
법을 이용한 내플라즈마성 코팅 증착

2022 년 8 월

서울대학교 대학원

재료공학부

이 재 후

# Plasma resistant coating using suspension plasma spraying and aerosol deposition

지도 교수 황 농 문

이 논문을 공학박사 학위논문으로 제출함  
2022 년 8 월

서울대학교 대학원  
재료공학부  
이 재 후

이재후의 공학박사 학위논문을 인준함  
2022 년 8 월

위 원 장 \_\_\_\_\_ 한 흥 남 (인)

부위원장 \_\_\_\_\_ 황 농 문 (인)

위 원 \_\_\_\_\_ 김 영 운 (인)

위 원 \_\_\_\_\_ 이 성 민 (인)

위 원 \_\_\_\_\_ 김 응 식 (인)

# Abstract

Here, the coating behavior of the YOF coating which was deposited by suspension plasma spraying was investigated using a high-output coaxial feeding method. Both the deposition rate and density of YOF coatings increased with the plasma power, which was determined by the gas ratio of Ar/H<sub>2</sub>/N<sub>2</sub> and the arc current. The coating thicknesses were  $58 \pm 3.4$ ,  $25.8 \pm 2.1$ ,  $5.6 \pm 0.6$ , and  $0.93 \pm 0.4$   $\mu\text{m}$  at plasma powers of 112, 83, 67, and 59 kW, respectively, for 20 scans with a feeding rate of the suspension at 0.045 standard liters per minute (slm). The porosities were  $0.15\% \pm 0.01\%$ ,  $0.25\% \pm 0.01\%$ , and  $5.50\% \pm 0.40\%$  at corresponding plasma powers of 112, 83, and 67 kW. High-resolution X-ray diffraction (HRXRD) shows that the major and minor peaks of the coatings which were deposited at 112 kW stem from trigonal YOF and cubic Y<sub>2</sub>O<sub>3</sub>, respectively. Increasing the flow rate of the atomizing gas from 15 slm to 30 slm decreased the porosity of the YOF coating from  $0.22\% \pm 0.03\%$  to  $0.07\% \pm 0.03\%$ . The Vickers hardness of the YOF coating containing some Y<sub>2</sub>O<sub>3</sub> deposited at

112 kW was  $550 \pm 70$  HV.

To develop the plasma-resistant coating of yttrium oxyfluoride using the suspension plasma spraying (SPS) process, a mixed  $Y_5O_4F_7/YF_3$  suspension was developed for fluorine-rich yttrium oxyfluoride coating. The undesired cubic and monoclinic  $Y_2O_3$  was formed in the yttrium oxyfluoride coating deposited with the  $Y_5O_4F_7$  suspension by the SPS process at atmospheric pressure. To minimize the formation of  $Y_2O_3$ , we inferred and proposed the mechanism of the SPS coating at atmospheric pressure and analyzed the coatings deposited by four suspensions with different mass ratios containing  $Y_5O_4F_7$  and  $YF_3$  particles. During the SPS process, the  $Y_5O_4F_7$  particles in the suspension reacted with hydrogen and oxygen through chemical reactions using the remaining thermal energy after the evaporation process, forming YOF and  $Y_2O_3$  composites near the surface of the coating. Using x-ray diffraction (XRD) and a high-resolution three-dimensional x-ray tomography microscope system (HR-XRM), a relatively large amount of  $Y_2O_3$  was found to have formed near the

surface of the coating deposited with the  $Y_5O_4F_7$  suspension, whereas the formation of  $Y_2O_3$  was minimized and the formation of yttrium oxyfluoride was maximized in the coating deposited with the mixed  $Y_5O_4F_7/YF_3$  suspension at a mass ratio of 7:3. This coating containing a minimum amount of  $Y_2O_3$  is expected to offer high plasma resistance.

To deposit a  $Y_5O_4F_7$  coating with better plasma resistance than YOF, aerosol deposition was studied.  $Y_5O_4F_7$  coatings were deposited on Al, sintered  $Al_2O_3$ , and C-plane sapphire substrates, and it was confirmed through XRD and SEM images analysis that all three samples formed dense coatings on the SEM images. Among them, the coatings deposited on the Al, sintered  $Al_2O_3$  substrates were black, while the coating deposited on the sapphire substrate was transparent. As a result of TEM analysis, it was confirmed that the black coatings had nano-cracks, whereas the transparent coating had no nano-cracks or nano-pores.

**Keyword :** plasma-resistance, suspension plasma spraying, yttrium oxyfluoride, aerosol deposition.

**Student Number :** 2017-24472

# Table of Contents

Chapter 1. Introduction .....	1
Chapter 2. Dense YOF coating deposited by suspension plasma spraying (SPS) .....	7
Chapter 3. Understanding YOF coating mechanism by SPS process and increasing YOF ratio.....	39
Chapter 4. $Y_5O_4F_7$ coating deposited by aerosol deposition (AD) .....	72
Bibliography .....	85
Abstract in Korean.....	99

# Chapter 1. Introduction

## 1.1. Plasma resistant coating

Flash memory is non-volatile storage, which means it retains stored data even when the power is turned off. NAND is one of the most common types of flash memory. NAND flash memory provides the advantages of a large storage capacity and significantly faster read/write response times [1]. Therefore, it is used in several types of storage devices, such as universal serial bus (USB) devices, solid-state drives (SSD), and digital cameras. In the semiconductor manufacturing industry, three-dimensional vertical NAND (3D V-NAND) technology, in which integrated circuit chips are vertically stacked in multiple layers, has been developed and is now mainly used in the manufacturing of NAND flash memory [2].

Recently, the dry etching process has been advanced in response to industrial needs to create high-level complex 3D

structures with a high aspect ratio (HAR) in scaling 3D V-NAND. To this end, the process is repeatedly performed in a harsh plasma environment in the semiconductor process chamber. The inner wall and other components of the chamber are subjected to high-power plasma during the stacking of multiple layers with HAR plasma etching, making them susceptible to plasma erosion and generating particles that act as contaminants [3, 4]. Fluorocarbon etching gases such as  $C_4F_8$ ,  $CHF_3$ , and  $C_3F_7OCH_3$  are mainly used in the etching process as plasma forming gases to etch silicon dioxide ( $SiO_2$ ) and silicon nitride ( $Si_3N_4$ ) [5].

To protect the inner wall and other parts in the chamber from fluorocarbon plasma etching and to suppress the generation of contaminants, coating methods involving chemically stable ceramic materials such as yttrium oxide ( $Y_2O_3$ ) and yttrium oxyfluoride (YOF) have been intensively studied.

## 1.2. Suspension plasma spraying

In the past, the atmospheric plasma spraying (APS) process was mainly used to apply plasma-resistant material coatings owing to its advantages of a low cost and high deposition rate. However, large micro-pores and cracks inevitably tend to form when coating with the APS process [6] because the size of the particles increases due to severe aggregation while feeding the particles into the plasma gun during the APS process, resulting in unstable feeding and non-melting or partial melting of large particles. Given that plasma-resistant material coatings require higher hardness and lower porosity for better plasma resistance, the suspension plasma spraying (SPS) method, which overcomes the disadvantages of the APS process, has been studied [7, 8, 9, 10]. The SPS process offers the advantage of being able to control the process precisely because it enables stable feeding of particles as small as  $2\ \mu\text{m}$  or less in a suspension, with the particles fully melted by the thermal energy of the

plasma flame [11].

Despite the advantage of SPS, it has a critical problem of consuming lots of energy in evaporating the solution. Because of this energy consumption, the power should be high enough to melt the particles that are suspended in the solution. However, the plasma power cannot be increased too high because of the gouging of the electrode.

To overcome this difficulty, we used the Axial III torch (Mettech), which has three cathodes and anodes with an axial feeding system. In this respect, the axial feeding has a much more advantage than the radial feeding commonly used in the SPS process due to the effective penetration of suspension into the core zone of the plasma jet. Besides, the high plasma power of the Axial III multi-electrodes has beneficial effects on particle melting and coating behavior.

In the SPS process, it was found that the quality of the suspension plays a critical role in the YOF coating. If the

$Y_5O_4F_7$  suspension is in poor conditions due to the severe flocculation, the suspension feeding would be unstable during the SPS process, and large pores and cracks may form in the YOF coating due to incomplete melting of the particles. In this study, the influence of the stability and particle size of the  $Y_5O_4F_7$  suspension on the YOF coating behavior was investigated to develop a suspension suitable for the dense YOF coating by the SPS process. Electrostatically and electrosterically stabilized aqueous  $Y_5O_4F_7$  suspensions were prepared and evaluated based on the wettability and dispersibility, which were compared with those of a commercially available  $Y_5O_4F_7$  suspension without dispersant. The optimum stabilization condition and formulations of the  $Y_5O_4F_7$  suspension for the dense YOF coating by the SPS process were determined.

### 1.3. Aerosol Deposition

Aerosol deposition is one of the methods for depositing

dense coatings at room temperature [12]. The aerosol deposition method that can obtain such a dense coating is used in various industries such as the semiconductor industry, solar cell, and SOFC [13~17].

Aerosol deposition process is as follows. The powder to be deposited is stirred and mixed with the carrier gas in the aerosol chamber to aerosolize, and then transferred to the deposition chamber by the gas flow generated by the difference in internal pressure between the two chambers, and then accelerated through the nozzle and deposited on the substrate. There are three main advantages of aerosol deposition: 1. Coating process proceeds at room temperature. 2. Dense film could be formed. 3. Compounds of complex composition could be deposited easily [19~24]. However, the mechanism of aerosol deposition is not clearly known. It is only explained by Dr. Akedo in the theory of room temperature impact consolidation (RTIC) [18~29].

# Chapter 2. Dense YOF coating deposited by suspension plasma spraying (SPS)

## 2.1. Introduction

Recently, it was discovered that, when the  $Y_2O_3$  coating layer reacts with fluorine plasma, an yttrium oxyfluoride (YOF) layer is formed on the surface, with this surface being highly plasma-resistant because it contains metal and fluorine components which are chemically stable. The enthalpy of formation of the metal-oxygen bond of YOF, the oxidized form of  $YF_3$ , which is  $-392 \text{ kJ}\cdot\text{mol}^{-1}$ , is smaller than that of  $Y_2O_3$ , which is  $-318 \text{ kJ}\cdot\text{mol}^{-1}$ . Therefore, YOF is more chemically stable than  $Y_2O_3$ . Moreover, the YOF layer can effectively inhibit particle generation [30,31].

It was also reported that YOF has a denser crystalline structure and thereby higher hardness and better corrosion resistance than  $YF_3$  [32]. Therefore, as a substitute for  $Y_2O_3$

and  $YF_3$ , YOF materials have attracted much attention. There are typically two ways to deposit YOF coatings: atmospheric plasma spraying (APS) and suspension plasma spraying (SPS). APS can produce a thick coating with high coating efficiency, but the coating tends to have numerous cracks and pores, making it vulnerable to plasma erosion [33]. SPS can overcome this disadvantage of APS, producing a dense coating [34,35,36]. Because the size of the feedstock particles in the droplet is as small as 10  $\mu\text{m}$  or less, the splat size of the coating layer can be assuredly small [37]. Because coating YOF with the SPS method is currently in its early stages, the properties of the YOF coating are scarcely known. To the best of our knowledge, YOF coatings have not yet been implemented in the manufacturing process of semiconductors, although tests are underway regarding their adoption.

Despite the advantage of SPS, it has a critical problem of consuming lots of energy in evaporating the solution. Because of this energy consumption, the power should be high enough to melt the particles that are suspended in the solution. However, the plasma power cannot be increased too high

because of the gouging of the electrode. To overcome this difficulty, we used the Axial III torch (Mettech), which has three cathodes and anodes with an axial feeding system. In this respect, the axial feeding has a much more advantage than the radial feeding commonly used in the SPS process due to the effective penetration of suspension into the core zone of the plasma jet. Besides, the high plasma power of the Axial III multi-electrodes has beneficial effects on particle melting and coating behavior.

## 2.2. Experimental methods

### 2.2.1. Suspension Plasma Spray (SPS) System

Suspension plasma spray equipment (Axial III, Mettech, Surrey, BC, Canada) is used to coat YOF coatings on two types of substrates. As shown in Figure 2.1, this equipment has the advantage of supplying the suspension to the plasma jet along the central axis of the plasma gun by axial feeding using a co-axial injector. When considering the penetration of

the suspension into the plasma jet and the heat transfer between the suspension and the plasma jet, axial feeding is more efficient than radial feeding, in which the suspension is supplied perpendicular to the plasma jet. Meillot et al. [22] reported that the coating efficiency is related to the suspension penetration into the plasma jet. As they used radial feeding, the coating efficiency was sensitive to the suspension injection pressure. However, with axial feeding, the axially supplied suspension can penetrate the core zone of the plasma jet, which makes the coating efficiency higher than that of radial feeding.

This equipment has three cathodes and anodes which are operated by three independent power supplies, which makes it possible to generate a high power without the cathodes being eroded by the plasma [23]. In this sense, this equipment has an advantage over the conventional plasma spray equipment, which typically has a single cathode and anode. Another advantage of this equipment is that the three plasma torch voltages fluctuate independently, which makes plasma gas velocity variations less sensitive to voltage fluctuations [22].

Typically, an Ar-N<sub>2</sub>-H<sub>2</sub> or Ar-N<sub>2</sub>-He gas mixture is used with possible electric power up to 120 kW. Argon was supplied in the direction perpendicular to the feeding line as an atomizing gas at a flow rate of 15 or 30 standard liters per minute (slm) in order to break up the droplets.

## 2.2.2. Feedstock Materials and Specimens

A commercial Y<sub>5</sub>O<sub>4</sub>F<sub>7</sub> suspension (Nippon Yttrium Co., Ltd., Omuta, Fukuoka, Japan) was used in the SPS coating process. The solvent is deionized water and the average size of the Y<sub>5</sub>O<sub>4</sub>F<sub>7</sub> particles is 3 μm with a suspension solid concentration of 10 wt.%. The plasma power and flow rate of the atomizing gas were varied to study their effects on the coating behavior of the YOF coatings. YOF coatings were deposited onto Al 6061 substrates of two different sizes of 10 mm<sup>3</sup> × 10 mm<sup>3</sup> × 10 mm<sup>3</sup> and 50 mm<sup>3</sup> × 50 mm<sup>3</sup> × 10 mm<sup>3</sup>. To improve the adhesion strength of the coatings, the surface of the Al substrate in each case was sandblasted to have a surface roughness average (Ra) value in the range of 2.3-2.8 μm by alumina particles (white fused alumina # 100,

Dae Han Ceramics Co., Ltd., Yeongam-gun, Jeollanam-do, Korea) less than 254  $\mu\text{m}$  in size. The Ra of the Al substrate was measured by surface roughness tester (MITUTOYO SJ-210, Kawasaki-shi, Kanagawa, Japan). Furthermore, the substrate was preheated with the plasma flame by scanning the entire surface of the substrate twice before the suspension was loaded onto the plasma jet. The temperature of the substrate was measured by a pyrometer (Fluke, 568 IR thermometer) and it was found to be 107 ° C immediately after the substrate was preheated, and the temperature of the substrate was measured to be 277 ° C immediately after the coating. The opposite side of the substrate was cooled by air at a distance of  $\sim 100$  cm in order to prevent the substrate damage due to the high-temperature plasma. We were guided by the reference [6] to choose the distance, which used the same Axial III plasma torch as our experiment. The air flux coming from the air gun was wide enough to cool the 10 mm<sup>3</sup>  $\times$  10 mm<sup>3</sup>  $\times$  10 mm<sup>3</sup> and 50 mm<sup>3</sup>  $\times$  50 mm<sup>3</sup>  $\times$  10 mm<sup>3</sup> substrates. The transverse speed of the plasma spraying gun was 1000 mm/s, and 20 coating cycles were used. For the 10

mm  $\times$  10 mm  $\times$  10 mm substrate, the horizontal and vertical spans of the gun trajectory were 460 and 40 mm, respectively. For the 50 mm  $\times$  50 mm  $\times$  10 mm substrate, the horizontal and vertical spans of the gun trajectory were 460 and 90 mm, respectively. The vertical increment of the gun position for every horizontal movement was 3 mm. The stand-off distance, referring to the distance between the gun and the substrate, was 50 mm. These conditions were chosen based on the literature [18,25].

### 2.2.3. Analysis Methods

For microscopic analyses: the coated surface in each case was cleaned with ethanol and the cross-section of the YOF coatings was fixed by hot mounting and polished to 1  $\mu$ m. A field-emission scanning electron microscope (FE-SEM, SU-70, Hitachi, Tokyo, Japan) was used to analyze the microstructure and morphology of the YOF coatings. The crystal structure of the YOF coatings was analyzed while using a high-resolution X-ray diffractometry (HRXRD, SmartLab, Rigaku, The Woodlands, TX, USA). An image

analysis program (ImageJ developed by the National Institutes of Health and the laboratory for Optical and Computational Instrumentation) was used to analyze the porosity of the cross-sections of the coatings [26].

In each case, the hardness of the coating was measured by a Vickers hardness tester (Duramin-40, Struers, Rotherham, UK) under a load of 200 gf (0.2 HV) and at a loading time of 10 s. Twelve indentations were made for the densest and thickest specimen, and the HV values were averaged after excluding the maximum and minimum values.

## 2.3. Results and Discussion

Regarding the choice of the gas mixture and the current, we were guided by the work of Kitamura et al. [6] and by our preliminary experiments. To determine the optimum condition based on this guidance, we used the four gas ratios of Ar/N<sub>2</sub>/H<sub>2</sub> of 90/54/36, 81/81/18, 100/100/0, and 140/60/0 standard liters per minute (slm) with respective currents of 230, 180, 230, and 200 A. Under these conditions, the

corresponding plasma powers were 112, 83, 67 and 59 kW, respectively. The suspension feeding rate was fixed at 45 standard cubic centimeters per minute (sccm). These and other processing parameters are shown in Table 1.

The noticeable differences in the conditions of Table 1a through Table 1d are the plasma power, which is related to the arc current, hydrogen gas fraction and total gas flow rate. Chakravarthy et al. [27] reported that the higher the plasma power is, the higher the plasma temperature becomes, which increases the temperature and the velocity of the injected particles. Therefore, a high plasma power causes the particles to melt better and allows for molten particles to spread and flow better on the surfaces of the substrates, increasing the coating thickness, decreasing the porosity, and improving the interfacial bonding. The hydrogen fraction of the total gas is the main parameter affecting the plasma power. In our experiment, the hydrogen fractions of the total gas in Table 1a-d were 20%, 10%, 0% and 0%, respectively. The higher the hydrogen fraction is, the higher the plasma power

becomes, as shown in Table 1. This is because H<sub>2</sub> has relatively high gas mass enthalpy and thermal conductivity values relative to those of other gases [28].

The total gas flow rate is related to the atomizing effect. The atomizing process fragments the liquid, making the droplet size smaller to allow for the particles to melt more easily. Atomizing is greatly affected by the Weber number (We), which is defined as the ratio of the aerodynamic force of the plasma gas to the surface tension of the liquid [29,30].

$$We = \frac{\rho_g \times u_r^2 \times d_l}{\sigma_l} \quad (1)$$

Here,  $\rho_g$  is the gas mass density (kgm<sup>-3</sup>),  $u_r$  is the relative velocity between the gas and liquid drop (ms<sup>-1</sup>),  $d_l$  is the diameter of the droplet or liquid jet (m), and  $\sigma_l$  (Nm<sup>-1</sup>) is the surface tension of the liquid.

Equation (1) indicates that the Weber number is proportional to the gas mass density and the square of the relative velocity of the liquid and gas and the mean diameter of the droplet. It is also inversely proportional to the surface tension of the liquid. The larger the Weber number is, the greater the

atomizing effect becomes. In Table 1, the surface tension of the liquid is identical in all four conditions and the droplet size might be similar among the four conditions because the total flow rates of the four conditions are similar. Therefore, the Weber number in Equation (1) would be proportional to the plasma gas density and square of the plasma gas velocity.

The information of the plasma gas density and velocity is needed to estimate the Weber number. The mass densities of the plasma gases Ar, N<sub>2</sub> and H<sub>2</sub> are 1.661, 1.165, and 0.0899 kg/m<sup>3</sup>, respectively. In Table 1a and b, the gas mixture contains H<sub>2</sub> with a low gas mass density, and the total flow rate, directly related to the gas velocity, is 180 slm, which is less than 200 slm, which is the total flow rate in Table 1c and d. Therefore, the Weber numbers under the conditions with a total gas flow rate of 180 slm are less than those under the conditions with a total gas flow rate of 200 slm and the atomizing effect in the latter is greater than those in the former.

As mentioned above, the plasma powers under the conditions

with a total gas flow rate of 180 slm were greater than those under the conditions with a total gas flow rate of 200 slm because hydrogen has higher gas mass enthalpy and higher thermal conductivity than other gases. In summary, the plasma powers in Table 1a,b are higher than those in Table 1c,d and the atomizing effects in Table 1a,b are weaker than those in Table 1c,d.

Although the Weber numbers predict that the process conditions of Table 1c,d produce denser and thicker coatings than those of Table 1a,b, the SEM images in Figure 2.2 and Figure 2.3 show that the coatings which are deposited under the conditions in Table 1a,b are denser and thicker than those deposited under the conditions in Table 1c,d. These results show that the plasma power is more effective than the atomizing effect with regard to particle melting.

Figure 2.2 shows cross-section images of YOF coatings deposited by SPS at different plasma powers. The coating thicknesses were  $58 \pm 3.4$ ,  $25.8 \pm 2.1$ ,  $5.6 \pm 0.6$ , and  $0.93 \pm 0.4 \mu\text{m}$  at plasma powers of 112, 83, 67 and 59

kW, respectively. The coating thickness was determined from cross-sectional SEM images and the thicknesses at ten points except for the maximum and minimum values which were averaged. The porosities were  $0.15\% \pm 0.01\%$ ,  $0.25\% \pm 0.01\%$  and  $5.50\% \pm 0.40\%$  at plasma powers of 112, 83 and 67 kW, respectively. The porosity was obtained from cross-sectional SEM images and the porosity values at five points were averaged. In this experiment, an Al substrate of 10 mm  $\times$  10 mm  $\times$  10 mm was used.

Figure 2.3 shows the higher magnification FESEM cross-sectional images of the sample shown in Figure 2.2.

Figure 2.4 shows the thickness and porosity of the YOF coating containing  $Y_2O_3$  as a function of plasma power. The coating thickness increased, and the porosity decreased with increasing plasma power.

The coating efficiency was estimated. The coating efficiency was regarded as the ratio of the mass of the deposited YOF coating containing  $Y_2O_3$  to the mass of the supplied  $Y_5O_4F_7$  particles in the suspension. The mass of the

coating was calculated to be 6.75 g, considering a plasma gun scan area of 46 cm × 5 cm, coating thickness of 58 μm, and density of the trigonal YOF of 5.06 g/mL [31]. The mass of the supplied Y<sub>5</sub>O<sub>4</sub>F<sub>7</sub> was calculated to be 15.75 g, considering a suspension feeding rate of 45 mL/min, a feeding time of 3.5 min, a density of the suspension of the deionized water of 1 g/mL, and a Y<sub>5</sub>O<sub>4</sub>F<sub>7</sub> particle concentration of 10 wt%. From these values, the coating efficiency was estimated to be approximately 42.9%.

When the coating is not thick enough, the measured hardness would be affected by the hardness of the substrate. For this reason, only the YOF coating, which was deposited at 112 kW, as shown in Figure 2.2a, was chosen for the hardness measurement. The Vickers hardness of the YOF coating, which contains some Y<sub>2</sub>O<sub>3</sub>, was 550 ± 70 HV. This hardness is much higher than 290 ± 30 HV for the YOF coating reported recently by Lin et al. [16], who deposited a dense, low-porosity (0.5%~1.0%) YOF coating by APS. On the other hand, Tsunoura et al. [4] reported that hot-pressed Y<sub>2</sub>O<sub>3</sub> and YOF bulks had respective hardness values of 683.2

HV and 693.4 HV. Therefore, the hardness levels of YOF coatings that were deposited by SPS and APS referred to above are ~20% and ~58% lower than that of the aforementioned hot-pressed YOF bulks, respectively. Considering that the porosity of YOF coatings is relatively low at  $0.14\% \pm 0.01\%$  for the YOF coating in Figure 2.2a and 0.5%-1.0% for the YOF coating reported by Lin et al. [16], the hardness of the YOF coating being lower than that of the hot-pressed bulk does not appear to stem mainly from the porosity. One possible reason for the lower hardness would be the lack of the exact stoichiometry of the YOF coating, which is attributed to the rapid solidification of the molten YOF.

When the suspension is atomized and divided into fine droplets at the plasma torch, the solvent should be evaporated. Approximately 25% of plasma jet enthalpy is consumed in the plasma because the evaporation process is endothermic [29]. After evaporation, the  $Y_5O_4F_7$  particles would be heated by the remaining thermal energy. If the remaining heat is not sufficient to melt the  $Y_5O_4F_7$  particles, they would remain in a solid form and most of them would then bounce off from the

substrate. In other words, non-melted  $Y_5O_4F_7$  particles would not contribute to the deposition, but fully or partially melted  $Y_5O_4F_7$  particles would do so. Therefore, as the plasma power is increased, the larger amount of  $Y_5O_4F_7$  particles would be melted and contribute to the deposition. As a result, the deposition rate increases. This would explain why the coating thicknesses in Figure 2.2 and Figure 2.3 increased with an increase in the plasma power.

There are several parameters affecting the porosity of the SPS coating such as droplet size, the size of particles in suspension, and incompletely melted particles [26]. Considering that the size of particles in suspension and the droplet size would be similar in all experimental conditions, the porosity of the SPS coating appears to mainly come from incompletely melted particles. Their amount would increase with decreasing plasma power. This would be why the porosity of the films in Figure 2.3 increased with decreasing plasma power. Therefore, the plasma power is critical and, in order to obtain thick and dense films by SPS, the plasma power should be high enough.

Figure 2.5a-d show the respective surface morphologies at plasma powers of 112, 83, 67 and 59 kW. The FESEM image presented in Figure 2.5a shows a microstructure consisting of smooth and rough areas. The smooth area would be splats which are formed from the spreading of molten droplets. The rough area would be formed either by fragments separated from the droplets when splashing on the growing surface or by incompletely melted particles. It should be noted that the total area of the smooth surface is much smaller in Figure 2.5d than in Figure 2.5a. This may stem from completely melted particles, which are far fewer in Figure 2.5d than in Figure 2.5a due to the low plasma power.

The crystalline structure of the YOF containing the  $Y_2O_3$  or  $Y_5O_4F_7$  coatings was investigated by X-ray diffraction (XRD), as shown in Figure 2.6. The major phase of trigonal YOF and minor phases of cubic  $Y_2O_3$  and monoclinic  $Y_2O_3$  were observed in the sample that was deposited at 112 kW (Figure 2.6a). On the other hand, Figure 2.6b shows that the peaks of the Al substrate mainly consist of minor peaks of

orthorhombic  $Y_5O_4F_7$  and trigonal YOF. Figure 2.6a shows that cubic and monoclinic  $Y_2O_3$  formed at the plasma power of 112 kW. With regard to the formation of  $Y_2O_3$ , Park et al. [32] reported that YOF powder started to lose fluorine in the form of  $YF_3$  at  $900^\circ\text{C}$  according to a thermogravimetric analysis, which was performed to study the high-temperature volatilization of YOF. Based on this result, they suggested that YOF can be volatilized in the form of  $YF_3$  in a plasma jet at  $\sim 5000^\circ\text{C}$  or higher. They also suggested that  $Y_2O_3$  is formed by the volatilization of  $YF_3$  from YOF.

Given that we used  $Y_5O_4F_7$  particles, the  $Y_2O_3$  in Figure 2.6a must have been formed from  $Y_5O_4F_7$ ,  $Y_5O_4F_7$  would not be directly transformed into  $Y_2O_3$  but would be initially transformed into YOF, after which the YOF would be transformed into  $Y_2O_3$ . Regarding the formation of YOF from  $Y_5O_4F_7$ , Biqu et al. [33] reported that, when  $Y_5O_4F_7$  was heat-treated, it transformed into YOF. According to our experiment, however, if  $Y_5O_4F_7$  was not sufficiently heated, it did not transform into YOF. For example, when the plasma power was 59 kW, which is relatively low, our XRD data in Figure 2.6b

showed that  $Y_5O_4F_7$  had major peaks and YOF had only minor peaks. Moreover, the coating thickness was only  $0.93 \pm 0.4$   $\mu\text{m}$ , as shown in Figure 2.2d. Considering the low growth rate at the power of 59 kW in Figure 2.2d and the major peaks of  $Y_5O_4F_7$  in Figure 2.6b, it appears that most of the  $Y_5O_4F_7$  particles did not melt and that the unmolten  $Y_5O_4F_7$  particles were not transformed into YOF, which would be attributed to the low volatilization rate of unmolten  $Y_5O_4F_7$  particles. To summarize,  $YF_3$  is volatilized from molten  $Y_5O_4F_7$  particles, transforming  $Y_5O_4F_7$  into YOF. Then,  $YF_3$  is further volatilized from YOF, which would produce  $Y_2O_3$  in Figure 2.6a. Although  $Y_2O_3$  is also known to be a plasma-resistant material, it is less resistant to plasma than YOF because  $Y_2O_3$  tends to react with the fluorine gas in the plasma and produce  $YF_3$  particles, which act as contaminants. In this sense, the formation of  $Y_2O_3$  is not desirable and it should be minimized, for which the volatilization rate of  $YF_3$  should be controlled. Systematic efforts would be needed to determine the optimum processing condition in order to minimize the formation of  $Y_2O_3$ . On the other hand, Figure 2.6b shows that the peaks of the Al

substrate mainly consist of a minor peak of orthorhombic  $Y_5O_4F_7$  without any peak of trigonal YOF. This would be attributed to the fact that the YOF coating was scarcely coated at 59 kW, as shown in the FESEM images in Figure 2.2d and Figure 2.3d. Because it is difficult to obtain quantitative information from the XRD data in Figure 2.6, we measured the compositions of Y, O, and F by EDS for the four coatings in Figure 2.2. These outcomes are shown in Table 2.

Table 2 shows that the atomic percentage of fluorine tends to decrease with an increase in the plasma power. This result supports our prediction that fluorine would be volatilized with an increase in the plasma temperature proportional to the plasma power. On the other hand, when considering that the atomic percentage of fluorine did not decrease above the plasma power of 83 kW, fluorine volatilization appears to be saturated above 83 kW.

As shown in Figure 2.7, EDS mapping of the coatings is qualitatively in agreement with the atomic percentage in Table 2. Fluorine, shown in green color, tends to decrease as the plasma power increases.

In the SPS process, the size of the droplets, which are formed as a result of atomizing inside the torch, can affect the coating behavior [9]. If the droplet size is large, a large amount of solvent must be evaporated. In addition, the number of particles contained in the large droplet would also be large, which would then make full melting difficult. The particles contained in each droplet would become agglomerated as the solvent evaporates. Because the incomplete melting of agglomerates would contribute to the porosity and decrease the coating rate, smaller droplets would be favorable for a dense coating and a high coating rate.

One way to decrease the size of droplets would be to increase the flow rate of the atomizing gas. Lee et al. [9] reported that the droplet size was  $\sim 1$  mm and a few hundred micrometers at the atomizing gas flow rates of 15 slm and 30 slm, respectively, because the atomizing gas flow rate affects the aerodynamic breakdown of the suspension. Because the maximum flow rate of an atomizing gas allowed in our equipment was 30 slm, we compared the coating behaviors using the two flow rates of 15 slm and 30 slm of the atomizing

gas. In this experiment, an Al substrate as large as 50 mm × 50 mm × 10 mm was used to confirm a uniform coating on a large-area substrate. Other experimental conditions were identical to those in Figure 2.2a, except for the plasma power of 103 kW.

Figure 2.8a,b show FESEM images of YOF coatings deposited at rates of 15 slm and 30 slm of the atomizing gas, respectively. The deposition was successfully done on the entire area of the substrate. A great difference in the coating thicknesses between Figure 2.8a,b could not be found. However, the coating in Figure 2.8b and Figure 2.9b, with porosity of  $0.07\% \pm 0.03\%$ , is denser than that in Figure 2.8a and Figure 2.9a, for which the porosity is  $0.22\% \pm 0.03\%$ . The lower porosity of the coating in Figure 2.8b and Figure 2.9b, as compared to that in Figure 2.8a and Figure 2.9a, implies that a higher percentage of the agglomerate contained in the droplet underwent full melting at 30 slm, more than at 15 slm of the atomizing gas. Because the incomplete melting of agglomerates is expected to decrease the coating rate, the coating in Figure 2.8b is expected to be thicker than that in

Figure 2.8a. However, the coating thickness in Figure 2.8a was very close to the value of  $\sim 25 \mu\text{m}$  shown in Figure 2.8b. In order to explain this result, it is assumed that 15 slm of atomizing gas would produce partially melted agglomerates rather than unmelted agglomerates and that the partially melted agglomerates would contribute to the deposition.

Parameters	Conditions			
	(a)	(b)	(c)	(d)
Electric power, kW	112	83	67	59
Ar/N <sub>2</sub> /H <sub>2</sub> flow rate (slm)	90/54/36	81/81/18	100/100/0	140/60/0
Total gas flow rate (slm)	180	180	200	200
Arc current (A)	230	180	230	200
Feeding rate (sccm)	45			
Atomizing gas flow rate (slm)	15			
Stand Off Distance (mm)	50			
Suspension concentration	10 wt. %			
Solvent	Deionized water			
Transverse speed	1000 mm/s			
Scan time (coating cycles)	20			
Substrate material	Al 6061			

**Table 2.1.** Processing parameters used during coating of YOF containing Y<sub>2</sub>O<sub>3</sub> or Y<sub>5</sub>O<sub>4</sub>F<sub>7</sub> by SPS.

Atoms (at.%)	(a) 112 kW	(b) 83 kW	(c) 67 kW	(d) 59 kW
Oxygen	46.39	44.57	39.45	28.46
Fluorine	24.09	22.16	30.15	43.42
Yttrium	29.52	33.27	30.40	28.12

**Table 2.2.** Compositions of YOF containing Y<sub>2</sub>O<sub>3</sub> or Y<sub>5</sub>O<sub>4</sub>F<sub>7</sub> measured by Energy-Dispersive X-ray Spectroscopy (EDS).

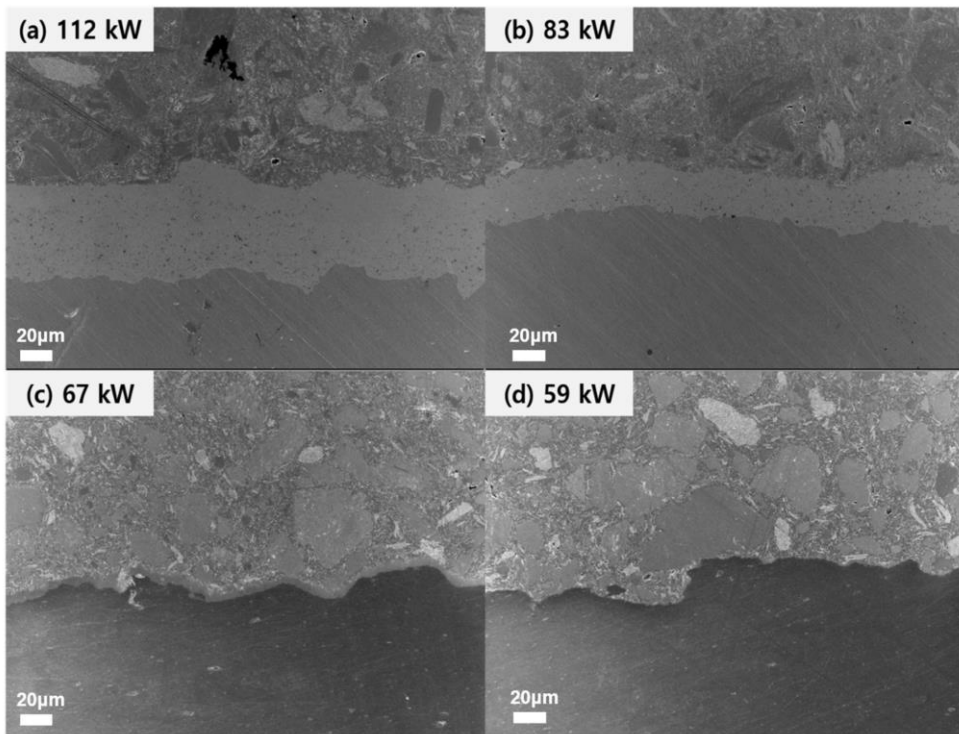


**Figure 2.2.** Cross-sectional FESEM images of YOF coatings deposited at plasma powers of (a) 112, (b) 83, (c) 67, and (d) 59 kW.

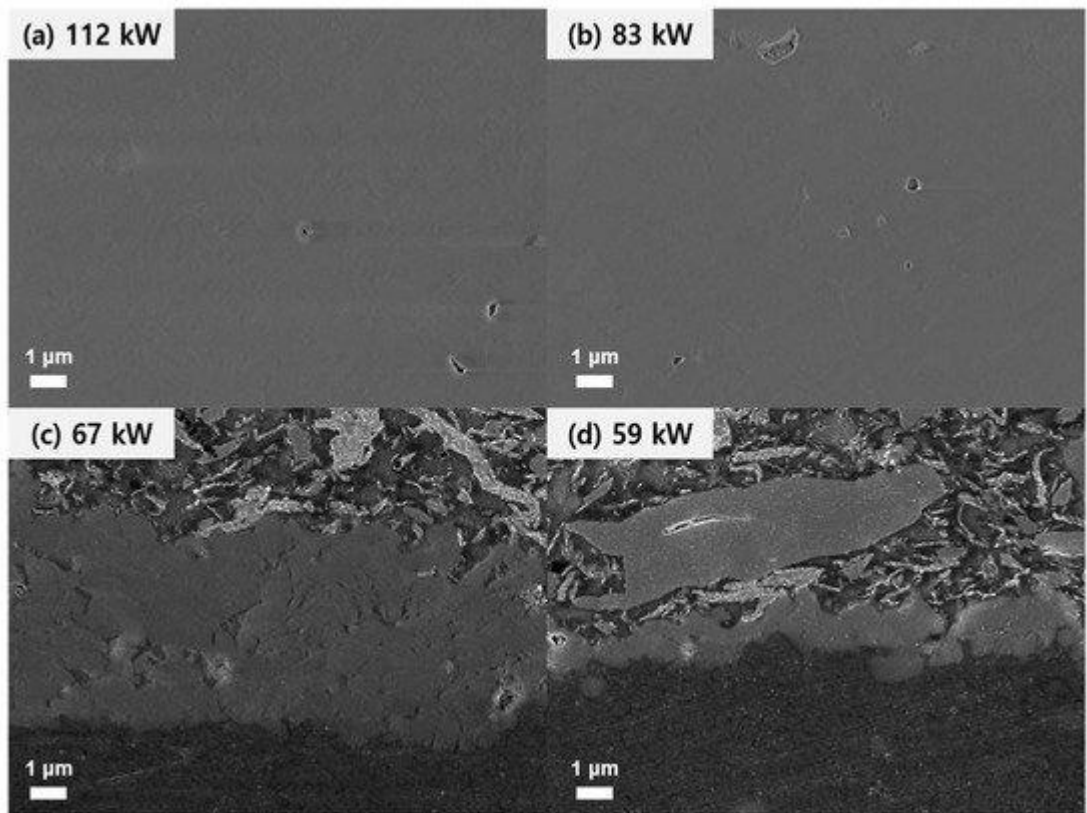


**Figure 2.3.** Higher magnification FESEM cross-sectional images of the sample shown in **Figure 2.2**.

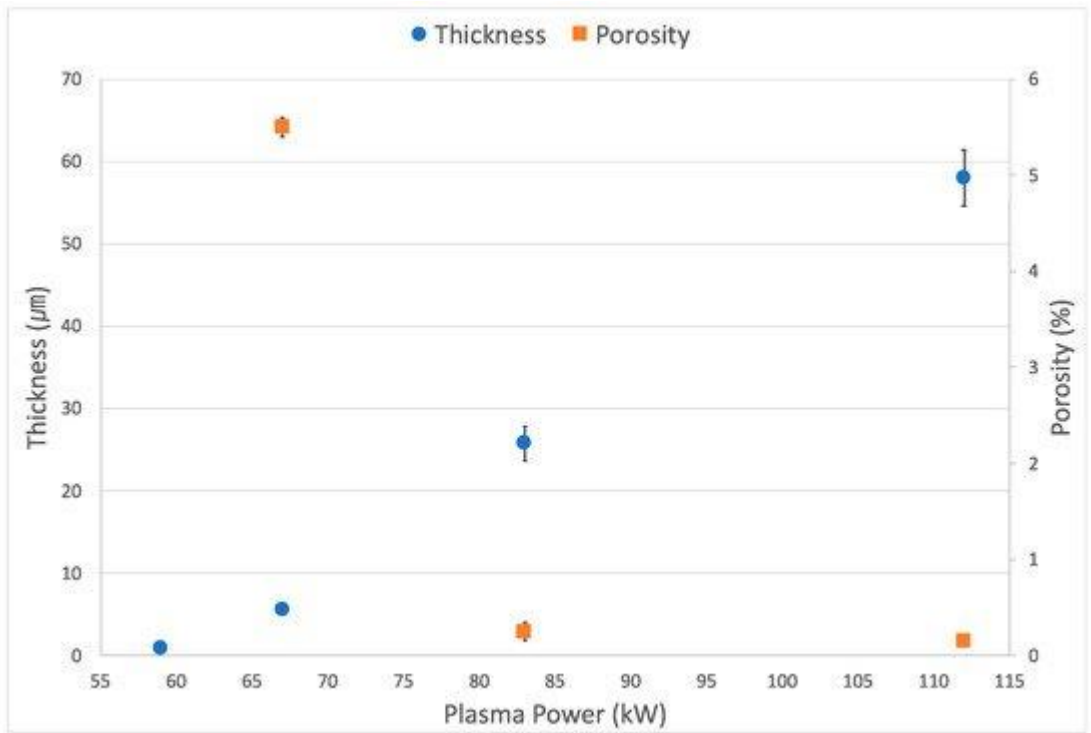


**Figure 2.4.** Thickness and porosity of the YOF coating containing  $Y_2O_3$  as a function of plasma power.

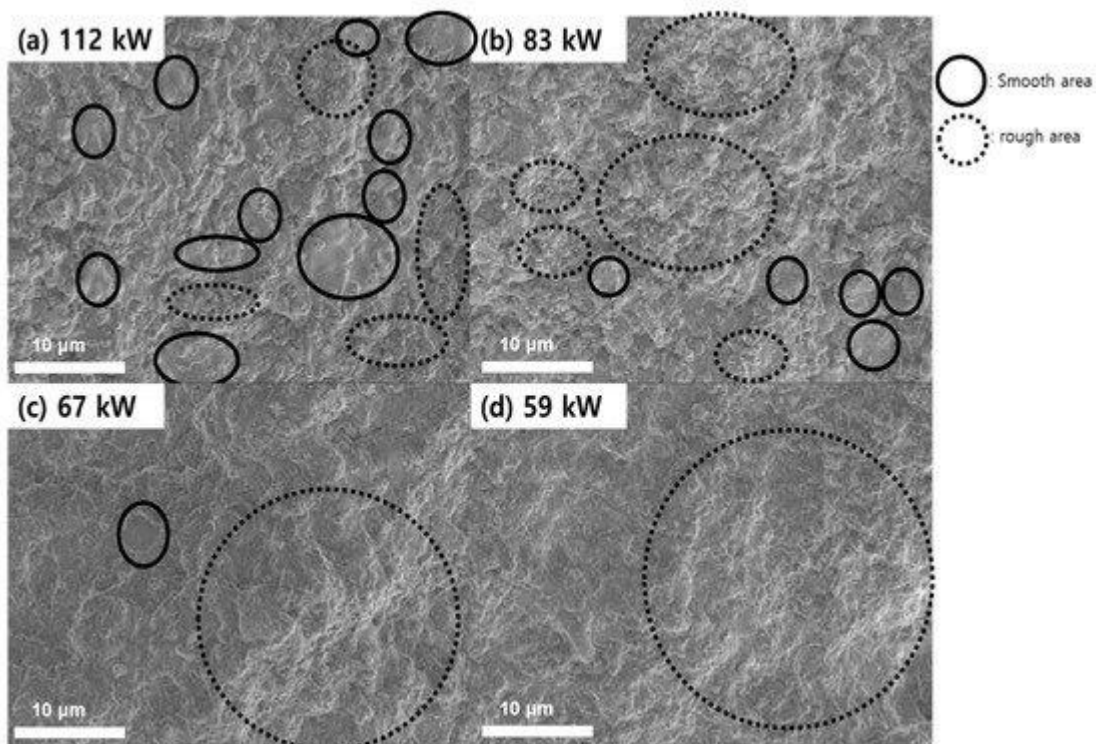
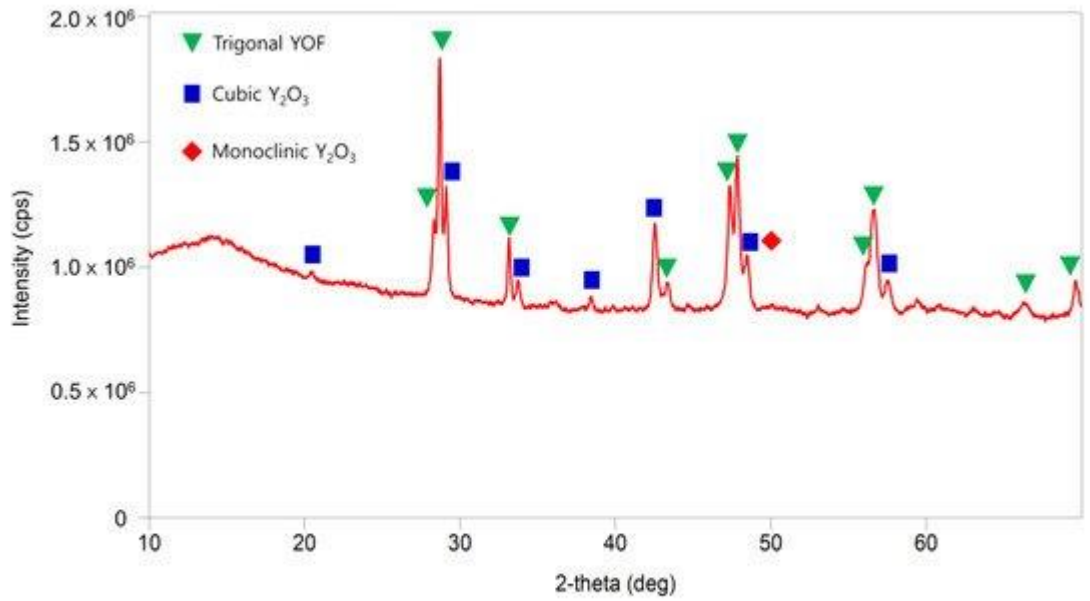
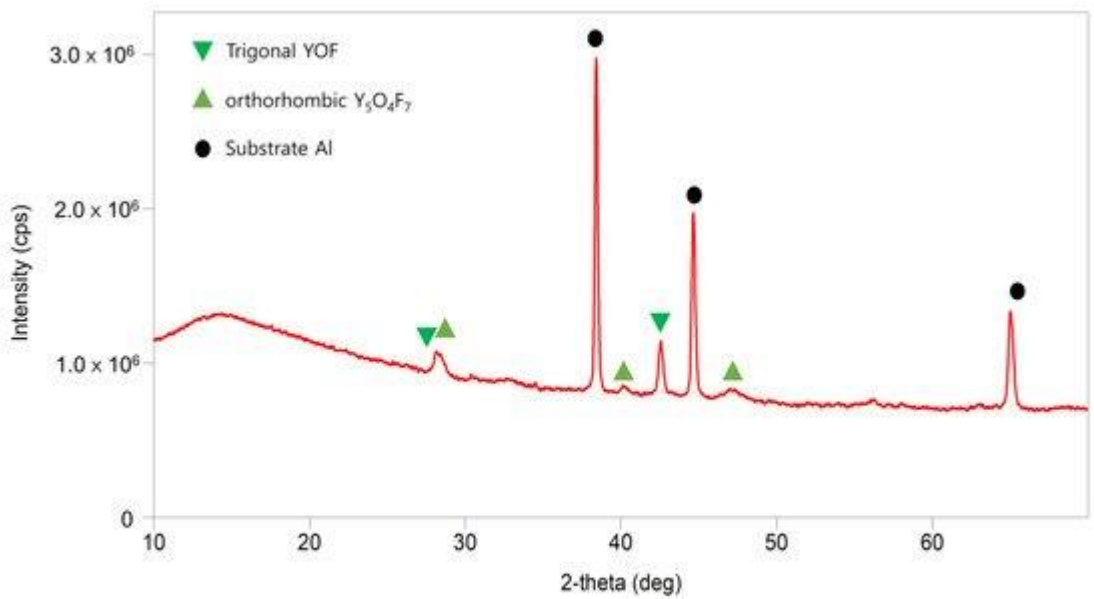


**Figure 2.5.** Surface FESEM images of YOF coatings deposited at plasma powers of (a) 112, (b) 83, (c) 67 and (d) 59 kW.



(a)



(b)

**Figure 2.6.** XRD patterns of YOF containing  $Y_2O_3$  or  $Y_5O_4F_7$  coatings deposited on Al substrates at plasma powers of (a) 112 kW and (b) 59 kW.

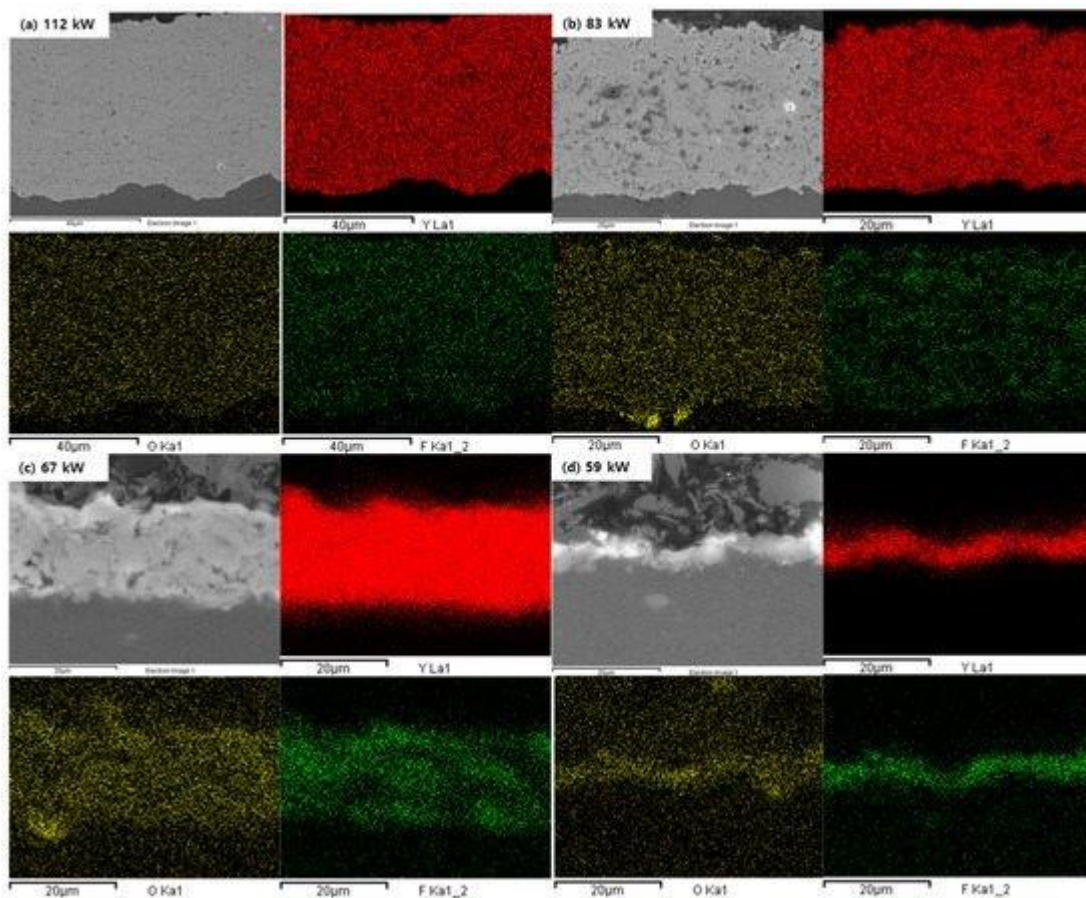


**Figure 2.7.** SEM-EDS elemental mappings of Y (red), O (yellow), and F (green) performed on the cross section of the YOF coatings containing  $Y_2O_3$  or  $Y_5O_4F_7$  deposited at (a) 112 KW, (b) 83 KW, (c) 67 KW, and (d) 59 KW.

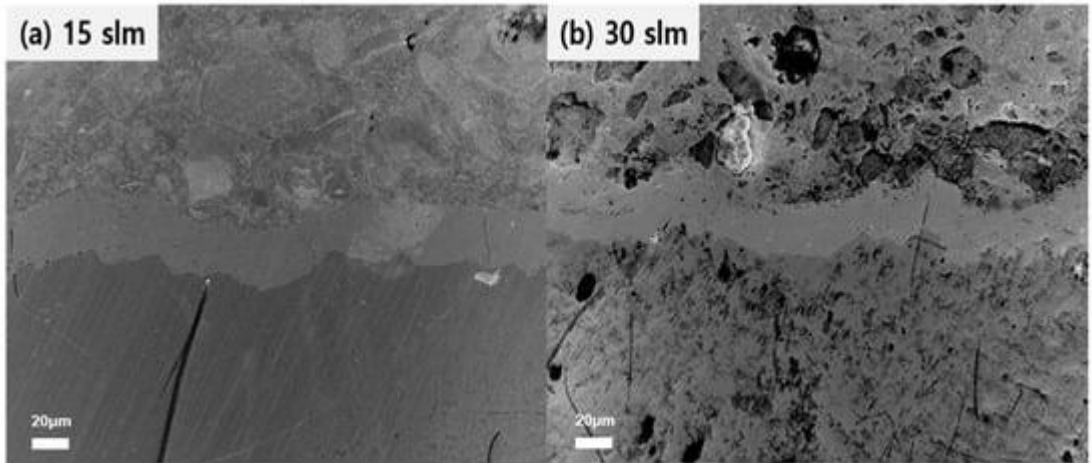


**Figure 2.8.** FESEM cross-sectional images of YOF coatings deposited on Al substrates by SPS at (a) 15 slm and (b) 30 slm of the atomizing carrier gas.

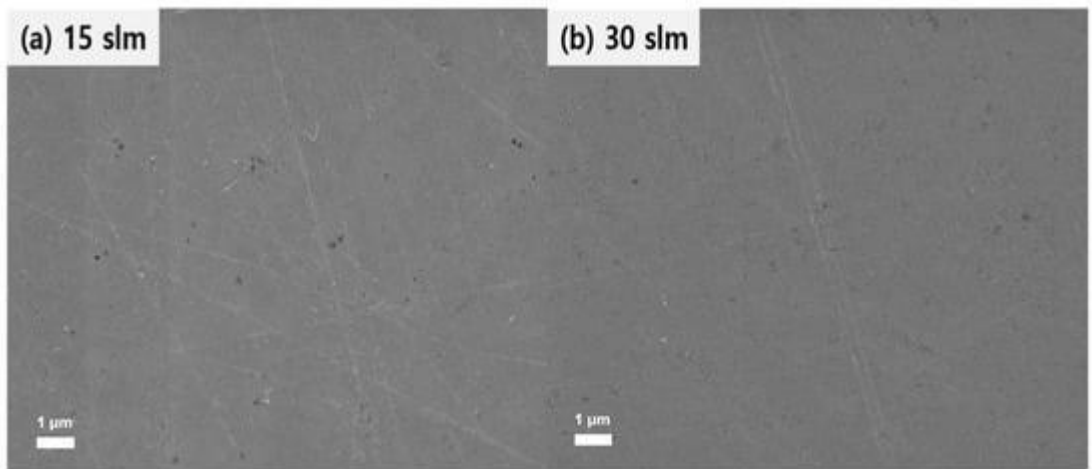


**Figure 2.9.** Higher magnification FESEM cross-sectional images of the sample shown in **Figure 2.8**.

# Chapter 3. Understanding YOF coating mechanism by SPS process and increasing YOF ratio

## 3.1. Introduction

In our previous works [7, 8], the SPS process was used to deposit a dense yttrium oxyfluoride coating with higher hardness and lower porosity levels than those of the APS process. In other work by the authors [42], an electrosterically stabilized  $Y_5O_4F_7$  suspension was developed in which nano-sized  $Y_5O_4F_7$  particles with a high zeta potential were stably dispersed. However, our previous work showed that unwanted cubic and monoclinic  $Y_2O_3$  formed in yttrium oxyfluoride coatings deposited with the  $Y_5O_4F_7$  suspension by the SPS process at atmospheric pressure [8]. When  $Y_2O_3$  is exposed to fluorocarbon plasma, particles such as yttrium fluoride ( $YF_3$ ) are generated by plasma etching during the process of the formation of a fluorination layer on the surface of the coating [13, 14]. The fluorination layer is formed when

oxygen is replaced through a redox reaction with fluorine on the surface of  $Y_2O_3$ , acting as a protection layer from the fluorocarbon plasma [7, 13]. We previously found that a dense fluorination layer formed beforehand on the surface of the YOF coating, with the binding energy between yttrium and oxygen higher than that of  $Y_2O_3$  [7]. For this reason, yttrium oxyfluoride is less affected by the reactive ion etching (RIE) of fluorocarbon plasma than  $Y_2O_3$  and thereby has better plasma resistance. If the unwanted  $Y_2O_3$  phase is formed mainly on the surface layer, it can be removed by grinding after the deposition process, though this adds to the cost. However, when the plasma-resistant material is coated on the round inner wall of the plasma etching chamber, the unwanted  $Y_2O_3$  phase cannot be removed by physical grinding and requires a chemical method, which would cost much more than physical grinding. Therefore, it is necessary to minimize the formation of  $Y_2O_3$  in the yttrium oxyfluoride coating by the SPS process. It is also necessary to study the mechanisms of the SPS coating process to understand why  $Y_2O_3$  forms. The purpose of this study is to determine the proper suspension

that best minimizes the formation of yttrium oxide or that maximizes the formation of yttrium oxyfluoride when coating with the SPS process. To do this, suspensions with different components were prepared using  $Y_5O_4F_7$  and  $YF_3$  particles, and coatings deposited by the SPS process were analyzed using x-ray diffraction (XRD) and high-resolution 3D x-ray tomography microscope (HR-XRM) imaging.

## 3.2. Experimental methods

### 3.2.1. Preparation of Suspensions

Commercial  $Y_5O_4F_7$  and  $YF_3$  powders (99.99%, Nippon Yttrium Co., Ltd., Omuta, Fukuoka, Japan) which were prepared by the fused and crushed method were used as a feedstock material. Figure 3.1 shows FE-SEM images of the  $Y_5O_4F_7$  and  $YF_3$  powders. The powders had a d50 agglomerate size of  $\approx 1.8 \mu\text{m}$ . Aqueous suspensions which consisted of  $Y_5O_4F_7$ ,  $YF_3$  or mixed  $Y_5O_4F_7/YF_3$  particles with a solid concentration of 10 wt.% were prepared using deionized water as a carrier fluid. Two types of mixed suspensions were

prepared with  $Y_5O_4F_7/YF_3$  at mass ratios of 7:3 and 5:5. The powders were dried in a drying oven for 24 hours at 110 C to minimize the tendency of agglomeration arising from powder humidity. An electrosteric dispersant (BYK-199, 1 wt.%) and a silicone-containing defoamer (BYK-019, 0.5 wt.%) were dissolved in deionized water. Subsequently, the dried powder was added to the dispersing medium. The dispersing medium was continuously and smoothly stirred to ensure penetration of the particles. High-intensity ultrasonication was then utilized to break down the particles in the suspension for 30 minutes to ensure stable wetting of the particles in the suspension, after which the suspensions were titrated with dilute KOH and HCl to have a pH of 8.6, offering optimized colloidal stability [32]. Although there are variations depending on the powders used, the pH of each suspension before titration was between 8.3 and 8.7, values that do not differ significantly from the target pH. However, as we wanted the SPS process to be performed under identical conditions, the pH of all suspensions was uniformly titrated to 8.6. The stabilized suspensions were stirred for more than 48 hours.

### 3.2.2. Suspension Plasma Spraying and Characterization of the Coatings

The coatings were deposited by SPS using an Axial III SPS system with coaxial feeding (Mettech' s Axial III, Northwest Mettech Corp., North Vancouver, BC, Canada), which has three separate power supplies with three single cathode–anode units. Inside the torch, three independent direct current arcs generated the three plasma jets, which converge to form a single integrated plasma jet. The torch configuration of the three spatially separated systems with three independent plasma generators enables coaxial feeding [15]. The suspension is injected directly into the plasma gun to minimize energy loss so that the heat generated from the plasma jet is transferred efficiently to the suspension, as shown in Fig. 3.2 [33]. The atomizing gas injection line is perpendicular to the feeding line. Nitrogen (N<sub>2</sub>) was supplied as atomizing gas to the feeding line to minimize the droplet size of the suspension by fragmenting it before the feedstock goes through the cathodes and anodes. It is well known that

the mixing of gas and liquid at the tip of the feeding line plays an important role in general radial feeding types of equipment. However, even if an atomizing gas is injected into the feeding line before the feedstock goes through the cathodes and anodes, it affects the improvement of the coating film density due to the atomization effect [35]. Therefore, the coating efficiency of this SPS system with coaxial feeding was higher than that of other SPS systems with a radial feeding system, as previously studied by the authors [38, 39]. The suspensions explained in the previous section were used to deposit coatings during the SPS process. During this process, the suspensions were vigorously agitated by an automated stirrer to prevent the particles from settling by gravity.

Al alloy 6061 with dimension of 10 x 10 x 5 mm<sup>3</sup> was used as a substrate. To enhance the adhesion strength of the coatings, the substrate was sandblasted to a surface roughness average (Ra) of 2.8 μm using alumina particles smaller than 257 μm. The substrate was held on a vice holder. Before the SPS coating process, the substrate was preheated

with the plasma flame by scanning the entire surface. The substrate was preheated to 490 K. During the SPS process, the substrate temperature increased due to the plasma flame and the flux of the heated particles. To avoid the melting of the substrate, the backside of the substrate was cooled with an air gun at a distance of 100 cm during the SPS process. The air flow from the air gun was wide enough to cool the entire substrate. After this process, the substrate temperature was measured and found to be 585 K using a pyrometer (568 IR thermometer, Fluke, Washington, USA). The processing parameters of the coatings are shown in Table 1.

On the other hand, HF gas was consistently produced during the SPS process. The SPS process was performed in an enclosed room, where the HF gas sensor was installed. The process room required appropriate ventilation and purification systems. During the process, the HF gas was evacuated so rapidly by ventilation and purification systems such that the spraying equipment was scarcely affected. Upon the completion of the SPS process, it was necessary to wait until the HF gas was exhausted to a safe level, as indicated by

a HF sensor.

Secondary electron (SE) image mode microscopy (FESEM, SU-70, Hitachi, Tokyo, Japan) was used to examine the cross-sectional microstructures and surface morphologies of the coatings. High-resolution x-ray diffractometry (HR-XRD, SmartLab, Rigaku, Austin, Texas, USA) was used to analyze the crystal structure of the coatings. A quantitative analysis of the coatings using Rietveld Refinement was conducted with the integrated x-ray powder diffraction software package PDXL (Rigaku (version 2.0), Austin, Texas, USA). To analyze the internal structures of the coatings, the three-dimensional (3D) visualization and top-view images by two-dimensional (2D) scanning from the surface to the depth direction of the coatings were obtained by a high-resolution 3D x-ray tomography microscope system (HR-XRM, Xradia 620 Versa, Carl Zeiss, California, USA) by expanding the region of interest (ROI) in the coatings to a specific ROI of  $500 \times 500 \times 100 \text{ } \mu\text{m}$ . The 3D visualization images were produced by the stacking of 2D scanning images. The image datasets of the internal structures of the coatings by HR-

XRM imaging were reconstructed and segmented using commercial software (Dragonfly software (version 2021.1), Object Research Systems (ORS), Montreal, Quebec, Canada). The hardness was measured by a Vickers hardness tester (Duramin-40, Struers, Cleveland, USA) under a load of 200 gf (0.2 HV) with twelve indentations on the polished coating surface. The porosity of the cross section of the coatings was analyzed using an image analysis program (ImageJ software (version 1.51k)) [42].

### 3.3. Results

Figure 3.3 shows FE-SEM cross-sectional images of the coatings deposited with  $Y_5O_4F_7$  (Fig. 3.3a), mixed  $Y_5O_4F_7/YF_3$  at a mass ratio of 7:3 (Fig. 3.3b), mixed  $Y_5O_4F_7/YF_3$  at a mass ratio of 5:5 (Fig. 3.3c), and the  $YF_3$  (Fig. 3.3d) suspension from the SPS process. The thicknesses of the coatings in Fig. 3.3(a), (b), (c), and (d) were  $34 \pm 1.5$ ,  $33 \pm 1.3$ ,  $39 \pm 1.9$ , and  $41 \pm 1.1$   $\mu\text{m}$ , respectively. The Vickers hardness values of the coatings in Fig. 3.3(a), (b), (c),

and (d) were  $493 \pm 55$ ,  $525 \pm 30$ ,  $458 \pm 60$ , and  $505 \pm 40$  HV0.2, respectively, with the corresponding porosities of the coatings being  $0.33\% \pm 0.01\%$ ,  $0.19\% \pm 0.01\%$ ,  $0.98\% \pm 0.02\%$ , and  $0.21\% \pm 0.01\%$ . The coatings deposited with mixed  $Y_5O_4F_7/YF_3$  at mass ratios of 7:3 and 5:5 in Fig. 3.3(b) and (c) had the lowest and highest porosities, respectively, which are closely related to the highest and lowest hardness values.

Figure 3.4 shows XRD patterns of the coatings shown in Fig. 3.3. The XRD peaks of the coatings deposited with  $Y_5O_4F_7$  suspension in Fig. 3.4(a) represented the crystalline structures of trigonal YOF, cubic  $Y_2O_3$ , and monoclinic  $Y_2O_3$  instead of the pure  $Y_5O_4F_7$  composition which was initially expected. In addition, the crystal structures of  $Y_5O_4F_7$  and  $YF_3$  are both orthorhombic at room temperature and are thus in the same phase. Thus, we initially expected that an orthorhombic  $Y_5O_4F_7/YF_3$  mixture coating would be formed at room temperature after deposition by the SPS process. However, the coatings deposited with the mixed  $Y_5O_4F_7/YF_3$  suspensions in Fig. 3.4(b) and (c) consisted of the crystalline

structures of trigonal YOF, orthorhombic  $Y_6O_5F_8$ , orthorhombic  $YF_3$ , and cubic/monoclinic  $Y_2O_3$  composites. Figure 3.4(c) shows that the coating deposited with the mixed  $Y_5O_4F_7/YF_3$  suspension (5:5) had the greatest variation of phases compared to the other coatings. Thus, it appears that the signal-to-noise ratio was low given the relatively low content in this case compared to the components of the other coatings.

The coatings deposited with the  $YF_3$  suspension in Fig. 3.4(d) consisted of only orthorhombic  $YF_3$  and  $Y_6O_5F_8$ . From these results, it was confirmed that all of the coatings deposited with each suspension could have a phase mixture different from the original phase of the particles in the suspension.

Figure 3.5 shows the relative percentages of composites in the coatings deposited with suspensions of different compositions as determined by the XRD analysis. The coating deposited with the  $Y_5O_4F_7$  suspension mainly consisted of trigonal YOF at 66 vol.%, and that with cubic/monoclinic  $Y_2O_3$  consisted of the highest percentage of

34 vol.% compared to the coatings deposited with other suspensions. On the other hand, when the coating was deposited with the mixed  $Y_5O_4F_7/YF_3$  (7:3) suspension, the orthorhombic  $Y_6O_5F_8$  was observed, and the percentage of YOF in the coating remained nearly constant with respect to the coating deposited with the  $Y_5O_4F_7$  suspension, while the percentage of  $Y_2O_3$  was significantly decreased by approximately 33% with respect to the coating deposited with the  $Y_5O_4F_7$  suspension. Meanwhile, when the mass ratio of 7:3 was changed to 5:5, i.e., when  $YF_3$  particles were slightly increased relative to  $Y_5O_4F_7$  particles in the suspension, it was observed that the percentage of trigonal YOF in the coating decreased by about 46% and that the percentage of cubic/monoclinic  $Y_2O_3$  rather increased by nearly 13% with respect to the coating deposited with the mixed  $Y_5O_4F_7/YF_3$  (7:3) suspension. On the other hand, the coating deposited with the  $YF_3$  suspension mainly consisted of orthorhombic  $YF_3$  at 74.2 vol.% and orthorhombic  $Y_6O_5F_8$  at 25.8 vol.%.

Figure 3.6 shows 3D visualized images of the top/side areas from the micron-scale HR-XRM of the coatings

deposited with the  $Y_5O_4F_7$  suspension (Fig. 3.6a), the mixed  $Y_5O_4F_7/YF_3$  suspension at a mass ratio of 7:3 (Fig. 3.6b), and the  $YF_3$  suspension (Fig. 3.6c) by the SPS process. These images were expanded to a specific ROI of the coating, reconstructed, and segmented with image-processing software to analyze the internal structure of the coatings. Each component of the composites could be segmented into different colors depending on the crystalline structure using the software. The images on the left, at the center, and on the right in Fig. 3.6(a), (b), and (c) represent, respectively, raw images of the coating, segmented images for each component, and images excluding other components except for a specific component in the coating. The segmented image visualizes the internal structure of the coatings, distinguishing by color-coding how each component was distributed.

In Fig. 3.6(a), the YOF and  $Y_2O_3$  composites can be identified by the blue and green colors, respectively. From the segmented images, it was confirmed that the composites of YOF and  $Y_2O_3$  were formed by chemical reactions during the SPS process at atmospheric pressure. In the coating deposited

with the mixed  $Y_5O_4F_7/YF_3$  suspension shown in Fig. 3.6(b), it was difficult clearly to identify each component in the composites because the amounts of  $Y_2O_3$  and  $Y_6O_5F_8$  were minute in comparison with the large amount of YOF. Clearly, the YOF shown in blue was the dominant phase. However, when other components were excluded except for  $Y_2O_3$  in the composites of each coating, it was observed that the amount of the  $Y_2O_3$  was clearly shown to be different between Fig. 3.6(a) and (b), a finding not clearly revealed in the segmented images. In other words, the amount of  $Y_2O_3$  in the coating deposited with the mixed  $Y_5O_4F_7/YF_3$  suspension was much lower than that in the coating deposited with the  $Y_5O_4F_7$  suspension. Meanwhile, in the coating deposited with the  $YF_3$  suspension in Fig. 3.6(c),  $YF_3$  and  $Y_6O_5F_8$  could be clearly identified, as indicated here in cyan and light green, respectively. These results by HR-XRM imaging were consistent with the previous results of the XRD analysis shown in Fig. 3.5.

Figure 3.7 shows HR-XRM 2D scanning top-view images from the surface to the inside of the coatings

deposited with the  $Y_5O_4F_7$  suspension (Fig. 3.7a), the mixed  $Y_5O_4F_7/YF_3$  suspension at a mass ratio of 7:3 (Fig. 3.7b), and the  $YF_3$  suspension (Fig. 3.7c) by the SPS process. The depth inside of the coatings of the HRXRM 2D scanning top-view images is approximately 15  $\mu\text{m}$  from the surface of the coatings. The images show the distribution of each component from the surface to the inside of the coating in a specific expanded ROI using a software program. Figure 3.8 shows the relative amount of each component near the surface and inside of the coating at the depth of approximately 15  $\mu\text{m}$  in a specific ROI calculated using the same software. Figure 3.7(a) shows that the YOF and  $Y_2O_3$  composites were distributed near the surfaces of the coatings and that the YOF was predominantly formed inside of the coating. In Fig. 3.8(a), the percentages of YOF and  $Y_2O_3$  near the surface were calculated as approximately 82 and 18%, while inside of the coating these outcomes were found to be 99 and 1%, respectively.

On the other hand, Fig. 3.7(b) shows that the YOF,  $YF_3$ , and  $Y_6O_5F_8$  composites were distributed near the surface of the coating deposited with the mixed  $Y_5O_4F_7/YF_3$  suspension.

Similar to Fig. 3.7(a), it was observed that YOF was predominantly formed inside of the coating. In Fig. 3.8(b), the calculated percentages of YOF,  $Y_6O_5F_8$ ,  $YF_3$ , and  $Y_2O_3$  near the surface of the coating were approximately 76, 8, 15, and 1%, while inside of the coating, they were 97, 1, 2, and almost 0%, respectively. It should be noted that the coating deposited with the mixed  $Y_5O_4F_7/YF_3$  suspension hardly had  $Y_2O_3$  but had mostly YOF near the surface and inside of the coating. For the coating deposited with the  $YF_3$  suspension, as shown in Fig. 3.7(c), the  $YF_3$  and  $Y_6O_5F_8$  composites were mainly distributed near the surface and  $YF_3$  was predominantly formed inside of the coating. In Fig. 3.8(c), the percentages of  $YF_3$  and  $Y_6O_5F_8$  near the surface of the coating were calculated and found to be about 77 and 23%, while inside of the coating they were approximately 99 and 1%, respectively. In all coatings shown in Fig. 3.7, the composites were distributed to a depth of  $11 \pm 1.1$   $\mu$ m from the surface, which corresponds to approximate coating thicknesses of  $32 \pm 2\%$ , as shown in Fig. 3.3.

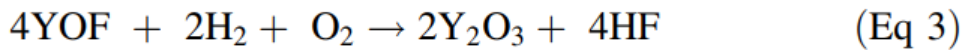
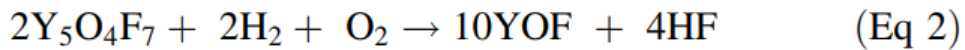
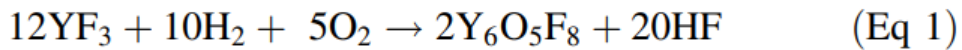
### 3.4. Discussion

In Fig. 3.3, the difference in the thickness of each coating under identical processing conditions indicates that the deposition rate depends on the composition of the suspensions. The density of  $Y_5O_4F_7$  is nearly 25% greater than that of  $YF_3$  ( $Y_5O_4F_7$ : 5.18 g/cm<sup>3</sup>,  $YF_3$ : 4.01 g/cm<sup>3</sup>). Hence, by comparing the thickness of each coating deposited with the  $Y_5O_4F_7$  suspension and the  $YF_3$  suspension at the same mass, it could be confirmed that the coating deposited with the  $YF_3$  suspension was thicker than that deposited with the  $Y_5O_4F_7$  suspension.

Figure 3.4 shows that the coatings deposited with each suspension had different phases. These results are attributable to the chemical reactions among the supplied particles ( $Y_5O_4F_7$ ,  $YF_3$ ), oxygen ( $O_2$ ) in the atmosphere, and hydrogen gas ( $H_2$ ), as illustrated in Fig. 3.9. Three reactions 1 to 3 with negative delta G value at high temperatures could be proposed and are shown below in terms of the reaction path and thermodynamic favorability [44, 47]. In general,  $H_2$

gas, which is a secondary gas for plasma formation, will be mostly dissociated, but during the SPS process, where a large amount of heat is consumed to evaporate the carrier fluid of the suspension, it could be deduced that  $H_2$  gas remained without being completely dissociated. Moreover, there is a possibility that the vaporized carrier fluid of the suspensions and the moisture ( $H_2O$ ) in the atmosphere were decomposed into hydrogen and oxygen by the thermal energy of the plasma flame, possibly participating in the chemical reactions [44]. For example, it is known that approximately 25% of the plasma jet enthalpy is consumed during the evaporation of the carrier fluid in the droplets [46]. In this context, upon deposition with the  $Y_5O_4F_7$  suspension, a significant amount of the thermal energy of the plasma flame would be consumed during the evaporation process of the carrier fluid in the droplets, and  $Y_5O_4F_7$  particles would melt due to the remaining thermal energy. Subsequently, the  $Y_5O_4F_7$  particles would react with hydrogen and oxygen through reactions 2 and 3 shown below, using the remaining thermal energy after the evaporation process. This explains why the coating deposited

with the  $Y_5O_4F_7$  suspension by the SPS process had a phase mixture different from the particles in the suspension. On the other hand, the coatings deposited with the mixed  $Y_5O_4F_7/YF_3$  suspensions by the SPS process were composed of YOF,  $Y_6O_5F_8$ ,  $YF_3$ , and  $Y_2O_3$  composites through reactions 1, 2, and 3 [47, 51]. The coating deposited only with the  $YF_3$  suspension was composed of  $YF_3$  and  $Y_6O_5F_8$  composites through reaction 1.



In Fig. 3.5, the percentage of  $Y_2O_3$  was significantly decreased in the coating deposited with the mixed  $Y_5O_4F_7/YF_3$  (7:3) suspension compared to the coating deposited with the  $Y_5O_4F_7$  suspension. As  $Y_5O_4F_7$  has not been studied much, its physical properties are not well known. What is known thus far is that both  $YF_3$  and  $Y_5O_4F_7$  have an orthorhombic structure with similar melting points (\* 1387 C). According to a recent

report by Tahara et al. [80], the specific heat capacity of  $\text{YF}_3$  is roughly 10% higher than that of  $\text{Y}_5\text{O}_4\text{F}_7$ . However, the latent heat is unknown for both  $\text{YF}_3$  and  $\text{Y}_5\text{O}_4\text{F}_7$ . Based on the physical properties and the experimental results, it could be inferred that  $\text{YF}_3$  added to the suspension has high thermal conductivity such that  $\text{Y}_6\text{O}_5\text{F}_8$  was generated through reaction 1. Also, the remaining residual heat was used to form YOF by the decomposition of  $\text{Y}_5\text{O}_4\text{F}_7$  in reaction 2, after which the formation of  $\text{Y}_2\text{O}_3$  by reaction 3 was drastically reduced due to the insufficient thermal energy required for the reaction. Therefore, if we use the mixed  $\text{Y}_5\text{O}_4\text{F}_7/\text{YF}_3$  suspension at a mass ratio of 7:3, it would be possible to form a coating that minimizes the percentage of yttrium oxide ( $\text{Y}_2\text{O}_3$ ) and increases the percentage of yttrium oxyfluoride (YOF,  $\text{Y}_6\text{O}_5\text{F}_8$ ).

Because plasma etching occurs on the surfaces of coatings, it is important to know precisely which components form near the surface of the coating in plasma-resistant coatings. For example, we found that the unwanted  $\text{Y}_2\text{O}_3$  component formed mainly near the surface of the coating

deposited with the  $Y_5O_4F_7$  suspension, as shown in Fig. 3.6(a), 7(a), and 8(a). This could be explained in terms of the chemical reactions described above. YOF on the surface of the coating formed through reaction 2 would have reacted with oxygen ( $O_2$ ) and hydrogen gas ( $H_2$ ) in the atmosphere. Then,  $Y_2O_3$  formed near the surface of the coating facing the atmosphere through reaction 3 proposed above using residual heat from the plasma flame after the SPS process. This phenomenon is unfavorable for plasma resistance in plasma-resistant coatings. On the other hand,  $Y_2O_3$  was scarcely observed near the surfaces of the coatings deposited with the mixed  $Y_5O_4F_7/YF_3$  (7:3) suspension compared to the coatings deposited with the  $Y_5O_4F_7$  suspension, as indicated in Fig. 3.6(b), 7(b), and 8(b), indicating that reaction 3 hardly occurred near the surface, as described above.

These results show that most of the minor phases in the coatings created by the SPS process were formed near the surface of the coating, further indicating that the minor phases inevitably formed at atmospheric pressure after the

Fig. 3.9 Schematic illustrating the formation mechanism of

$Y_2O_3$  during the SPS coating at atmospheric pressure 1518 J Therm Spray Tech (2022) 31:1508–1520 123 SPS process. It is presumed that the chemical reactions between the surface of the coating and the atmosphere occurred actively by the residual heat caused by the high thermal energy of the plasma flame immediately after the SPS process. Therefore, to minimize the formation of  $Y_2O_3$  or to maximize the formation of YOF or  $Y_6O_5F_8$  near the surface of the coating, it would be more advantageous to supply the mixed  $Y_5O_4F_7/YF_3$  (7:3) suspension rather than the  $Y_5O_4F_7$  suspension for a fluorine-rich yttrium oxyfluoride coating.

### 3.5 Conclusion

A mixed  $Y_5O_4F_7/YF_3$  suspension to minimize the formation of  $Y_2O_3$  was developed for a fluorine-rich yttrium oxyfluoride coating material by the SPS process at atmospheric pressure. According to XRD and HR-XRM imaging analyses, it was inevitable that undesired composites containing such as  $Y_2O_3$  on the surfaces of the coatings would

form due to the chemical reactions occurring during the SPS process at atmospheric pressure. A large amount of  $Y_2O_3$  formed near the surface of the coating deposited with the  $Y_5O_4F_7$  suspension, whereas the formation of  $Y_2O_3$  was minimized and the formation of YOF or  $Y_6O_5F_8$  increased further in the coating deposited with the mixed  $Y_5O_4F_7/YF_3$  suspension at a mass ratio of 7:3. Therefore, the yttrium oxyfluoride coating deposited with the mixed  $Y_5O_4F_7/YF_3$  suspension at a mass ratio of 7:3 by the SPS process at atmospheric pressure is expected to have superior plasma resistance compared to this capability of the coating deposited with the suspension composed of only  $Y_5O_4F_7$  particles.

Parameters	Conditions
Electric power (kW)	92
Ar/N <sub>2</sub> /H <sub>2</sub> flow rate (standard liter per minute (slm))	90/54/36 (5:3:2 ratio)
Total gas flow rate (slm)	180
Arc current (A)	230
Feeding rate (standard cubic centimeter per minute (sccm))	40
Atomizing gas flow rate (slm)	30
Stand off Distance (mm)	50
Traverse speed (mm/s)	1000
Scan time (coating cycles)	20
Coating time (min)	3

**Table 3.1.** Processing parameters for the coatings by the SPS process

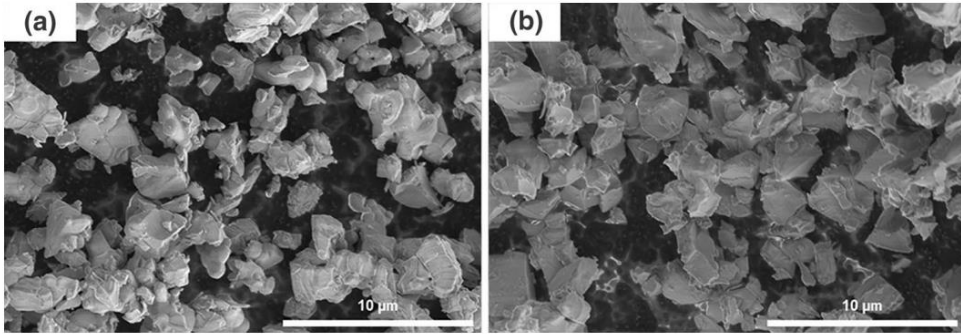


**Figure 3.1.** FESEM images of the powders (a)  $Y_5O_4F_7$  (b)  $YF_3$

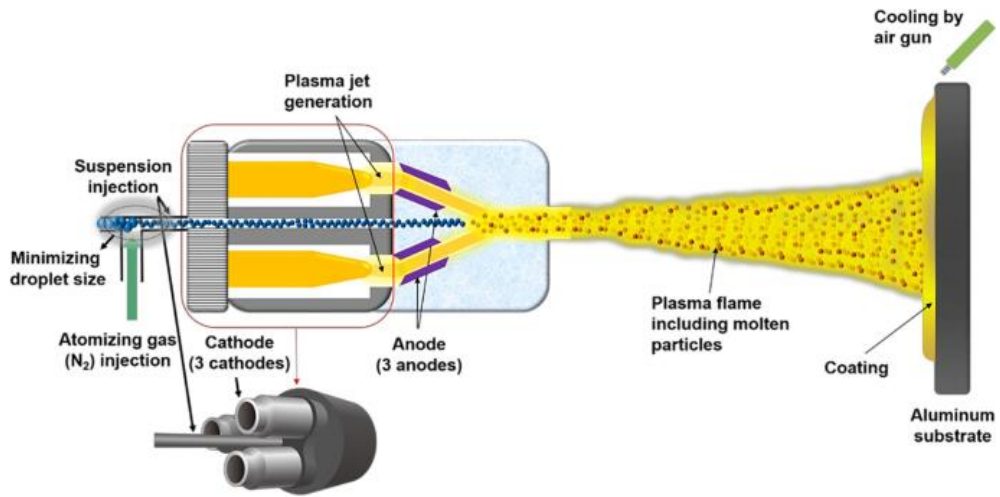
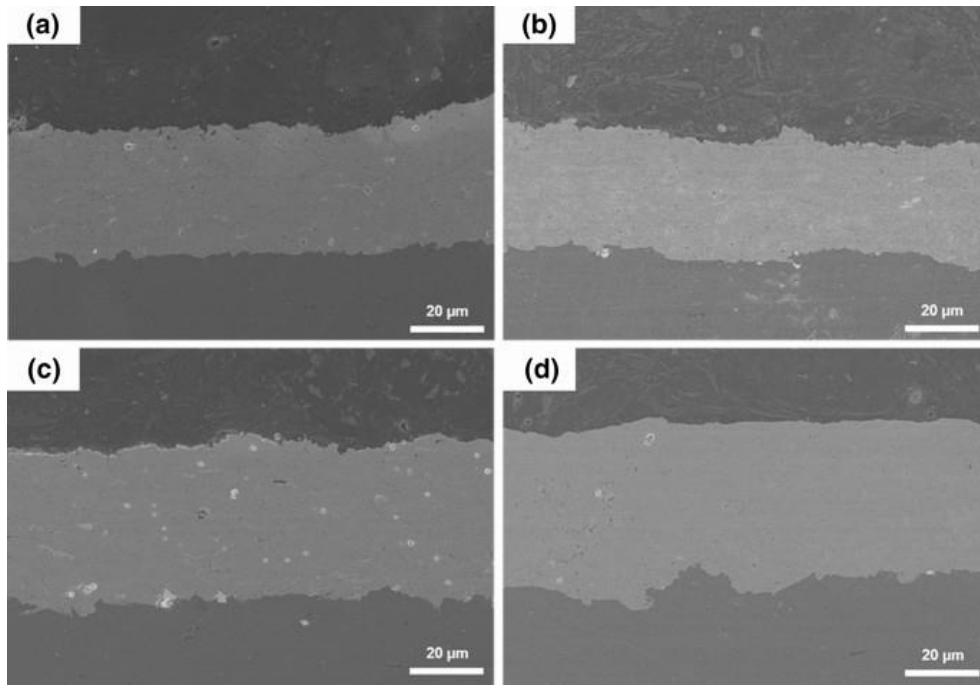
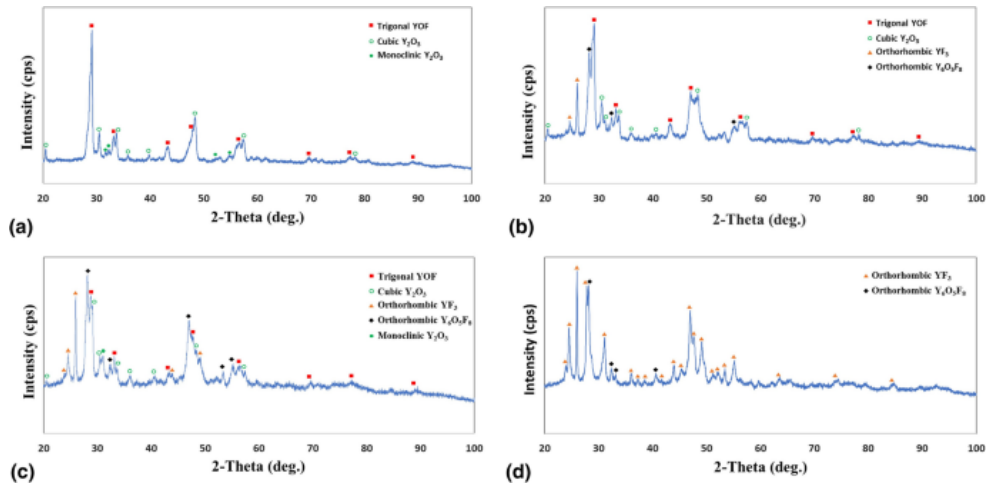


Figure 3.2. Schematic of the Axial III SPS system [9]

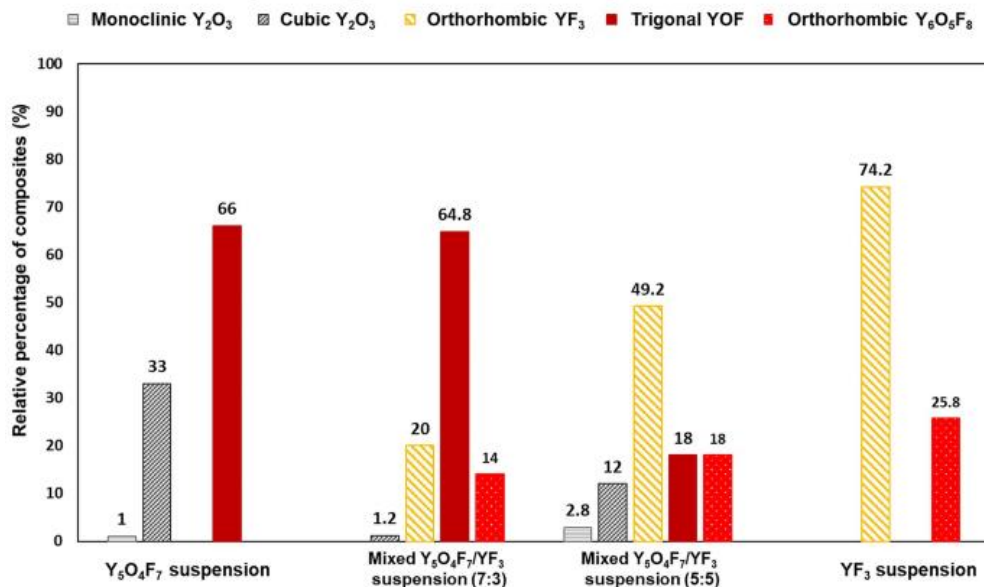


**Figure 3.3.** FE-SEM cross-sectional images of the coatings deposited with (a)  $Y_5O_4F_7$ , (b) mixed  $Y_5O_4F_7/YF_3$  (7:3), (c) mixed  $Y_5O_4F_7/YF_3$  (5:5), and (d)  $YF_3$  suspension by the SPS process



**Figure 3.4.** XRD patterns of the coatings deposited with (a)  $Y_5O_4F_7$ , (b) mixed  $Y_5O_4F_7/YF_3$  (7:3), (c) mixed  $Y_5O_4F_7/YF_3$  (5:5), and (d)  $YF_3$  suspension by the SPS process

(a) Distribution according to the crystal structure of each component



(b) Distribution of the total amount of each component

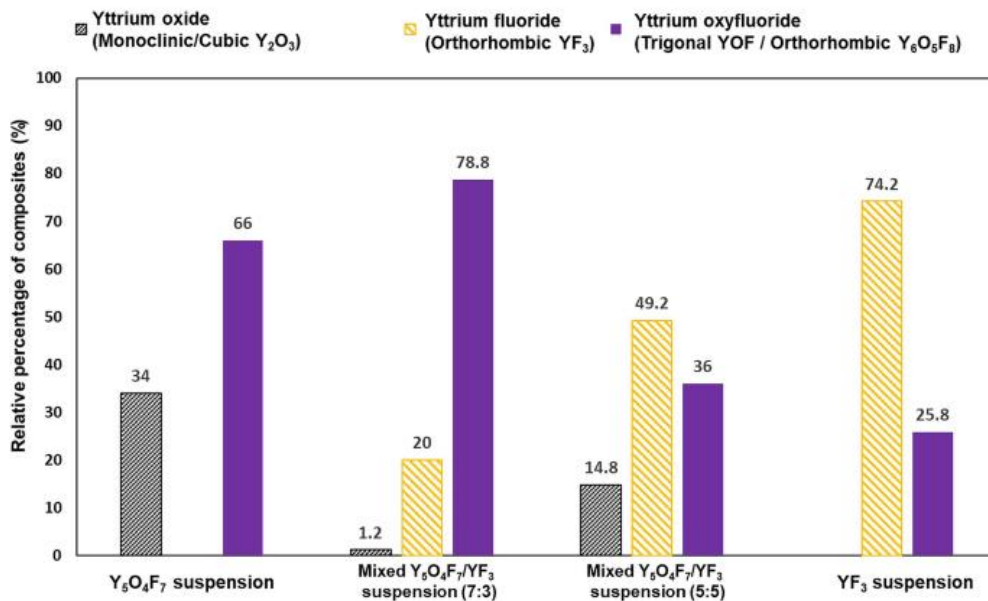
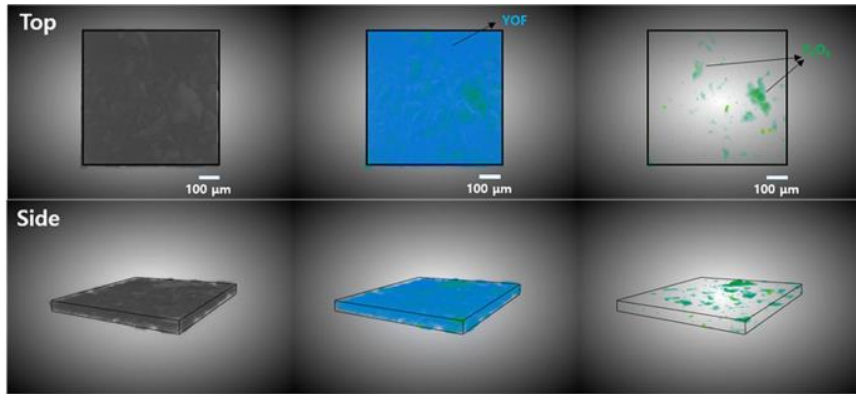
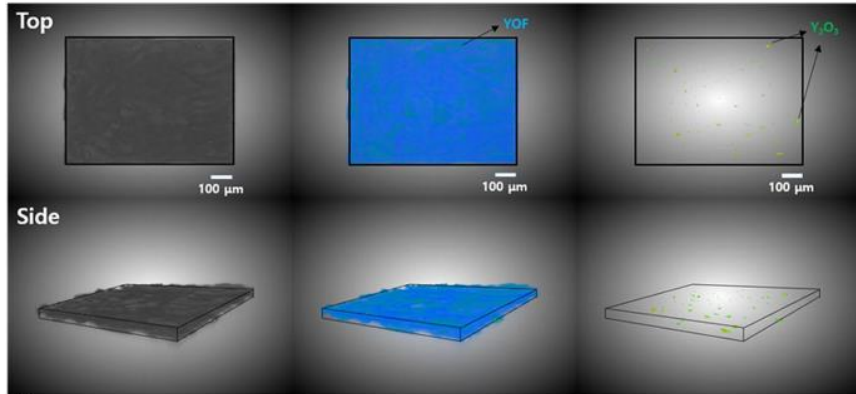


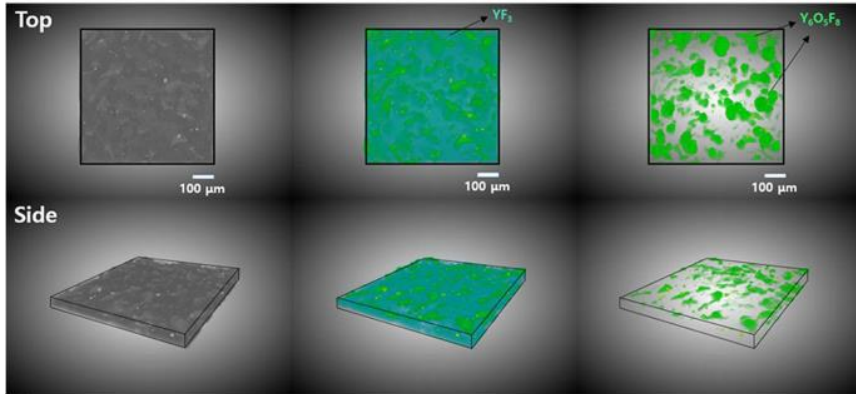
Figure 3.5. Relative percentages of composites in the coatings (a) according to the crystalline structure and (b) those of the total amount of each component deposited with  $Y_5O_4F_7$ , mixed  $Y_5O_4F_7/YF_3$  in a mass ratio of 7:3, mixed  $Y_5O_4F_7/YF_3$  in a mass ratio of 5:5, and  $YF_3$  suspensions by the SPS process at atmospheric pressure



(a)



(b)



(c)

**Figure 3.6.** HR-XRM 3D visualized top/side view images of the coating deposited with (a)  $Y_5O_4F_7$  suspension, (b) mixed  $Y_5O_4F_7/YF_3$  suspension in a mass ratio of 7:3, and (c)  $YF_3$  suspension by the SPS process at atmospheric pressure

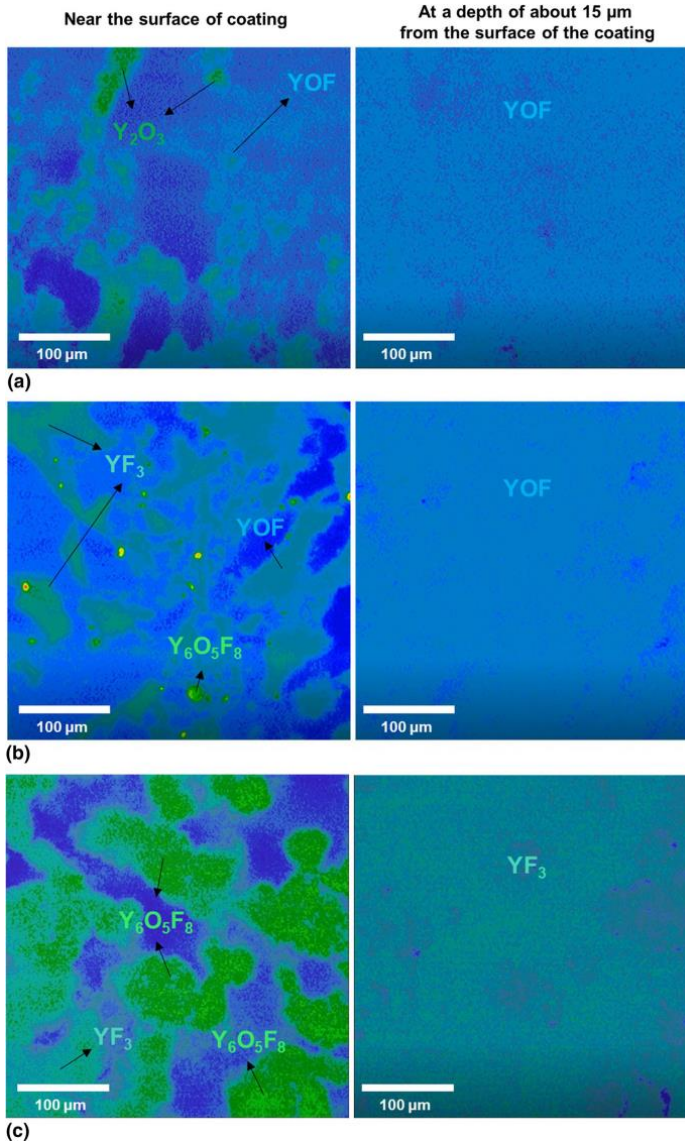


**Figure 3.7.** HR-XRM 2D scanning top-view images from the surface to the inside of the coatings deposited with (a)  $Y_5O_4F_7$  suspension, (b) mixed  $Y_5O_4F_7/YF_3$  suspension in a mass ratio of 7:3, and (c)  $YF_3$  suspension by the SPS process

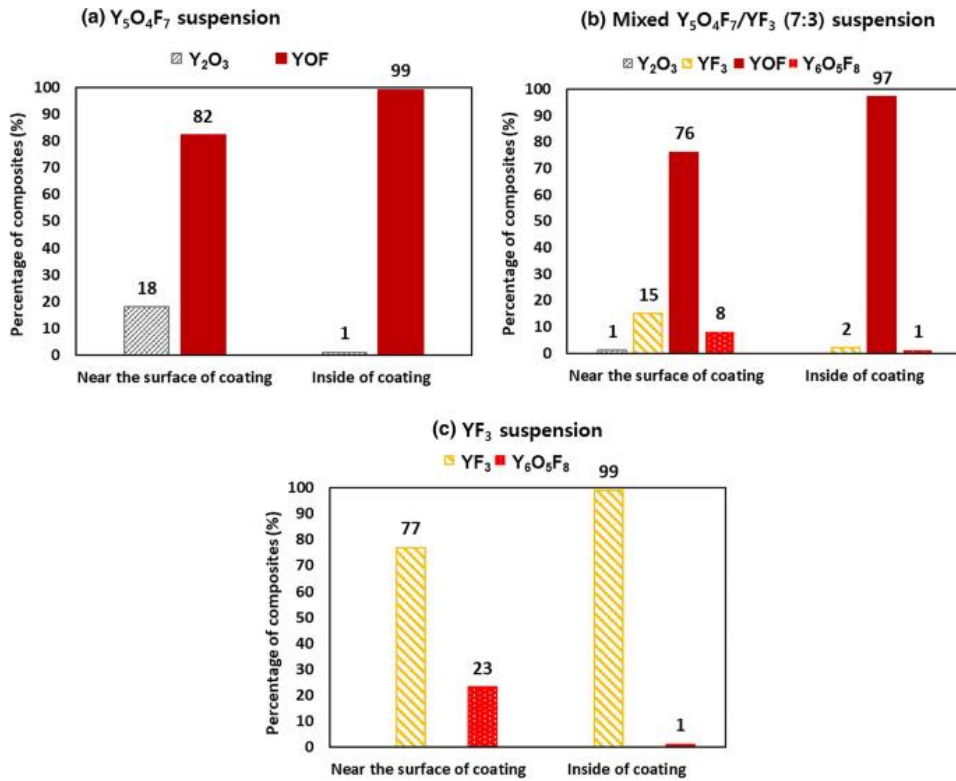


**Figure 3.8.** Percentages of the composites near the surface and inside of the coatings at the depth of about 15  $\mu\text{m}$  analyzed by HR-XRM 2D scanning in a specific ROI

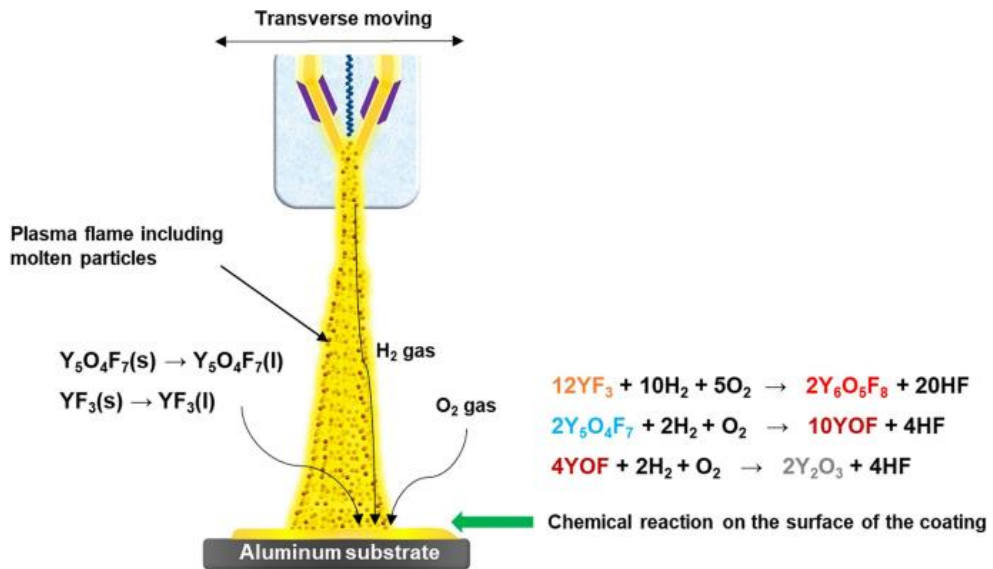


**Figure 3.9.** Schematic illustrating the formation mechanism of  $Y_2O_3$  during the SPS coating at atmospheric pressure

# Chapter 4. $Y_5O_4F_7$ coating deposited by aerosol deposition (AD)

## 4.1. Introduction

Aerosol deposition is one of the methods for depositing dense coatings at room temperature [12]. The aerosol deposition method that can obtain such a dense coating is used in various industries such as the semiconductor industry, solar cell, and SOFC [13~17].

Aerosol deposition process is as follows. The powder to be deposited is stirred and mixed with the carrier gas in the aerosol chamber to aerosolize, and then transferred to the deposition chamber by the gas flow generated by the difference in internal pressure between the two chambers, and then accelerated through the nozzle and deposited on the substrate. There are three main advantages of aerosol deposition: 1. Coating process proceeds at room temperature. 2. Dense film could be formed. 3. Compounds of complex composition could be deposited easily. However, the mechanism of aerosol deposition is not clearly known. It is

only explained by Dr. Akedo in the theory of room temperature impact consolidation (RTIC) [18].

## 4.2. Experimental procedure

A schematic of the AD reactor used in this experiment is shown in Fig. 4.1.  $N_2$  as the carrier gas was passed through the vibrating aerosol generation unit carrying a fine ceramic powder. The particle-laden flow was accelerated through the converging type nozzle with orifice and inlet sizes of  $5 \times 1 \text{ mm}^2$  and  $10 \times 8 \text{ mm}^2$ , respectively, and collided with substrates connected to the stage, forming a dense film. Orthorhombic  $Y_5O_4F_7$  powder with an average size of  $2.0 \mu\text{m}$  was used as a feedstock material as shown in Fig. 4.2. The velocity of the particle was controlled by the flow rate of the  $N_2$  carrier gas, which was 7 L per min (LPM). During the process, the pressure inside the deposition chamber was kept below 1 Torr, and the stand-off distance between the nozzle orifice and substrate was controlled within 1 mm.  $Y_5O_4F_7$  coatings were deposited onto Al, sintered  $Al_2O_3$ , and C-plane sapphire substrates of size of  $10 \text{ mm} \times 10 \text{ mm} \times 0.43 \text{ mm}$ .

The cross-section and surface images of coatings were analyzed by field emission scanning electron microscopy (FE-SEM, SUPRA, Carl Zeiss) and high-resolution TEM (HRTEM, F20, Tecnai), respectively. Selected area electron diffraction (SAED) patterns were observed to examine the crystallinity of films and particles. High-resolution x-ray diffractometry (HR-XRD, SmartLab, Rigaku, Austin, Texas, USA) was used to analyze the crystal structure of the coatings.

### 4.3. Results and Discussion

Figure 4.3 shows  $Y_5O_4F_7$  coatings deposited on Al, sintered  $Al_2O_3$ , and C-plane sapphire, respectively. Figure 4.4 shows that the  $Y_5O_4F_7$  coating on the sapphire substrate is transparent. Figure 4.5 is a FESEM cross-sectional image of the  $Y_5O_4F_7$  coating on Al, sintered  $Al_2O_3$ , and sapphire substrates (a), (b), and (c) respectively. All three samples have a thickness of about 1.3  $\mu m$  and a porosity of less than 0.1%, confirming that the coating is dense. Figure 4.6 shows

the results of XRD analysis of three samples. Each coating is Orthorhombic  $Y_5O_4F_7$ . The Fast Fourier Transform (FFT) analysis result through TEM in Figure 4.7 also shows that it has an orthorhombic  $Y_5O_4F_7$  structure. Figure 4.7 shows TEM cross-sectional images of three samples. As shown in the TEM image, white nano cracks exist in samples (a) and (b), and no nano cracks or nanopores exist in sample (c). From this, it is presumed that the black color of the  $Y_5O_4F_7$  coating in samples (a) and (b) is due to light scattering due to nano cracks inside the coating.

#### 4.4. Conclusion

Through aerosol deposition and 2  $\mu\text{m}$  of  $Y_5O_4F_7$  powder, we succeeded in depositing a dense  $Y_5O_4F_7$  coating with a porosity of less than 0.1% on Al,  $Al_2O_3$ , and sapphire substrates. We succeeded in depositing a dense and transparent coating.



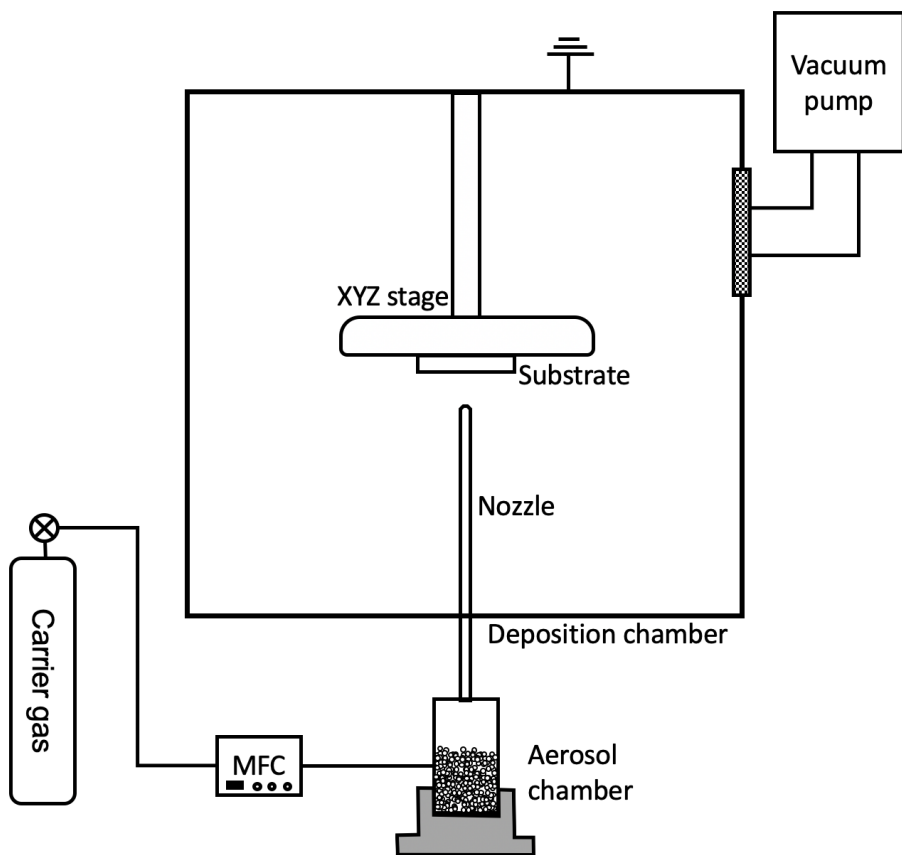


**Figure 4.1.** schematic of AD system

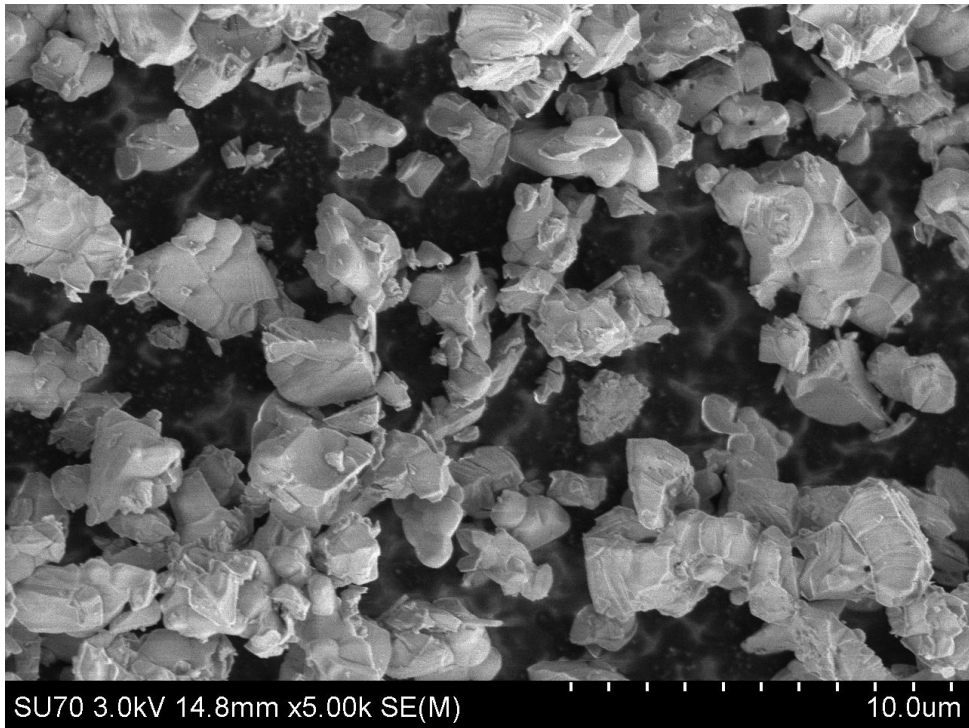


**Figure 4.2.** FE-SEM image of 2  $\mu\text{m}$   $\text{Y}_5\text{O}_4\text{F}_7$  powder

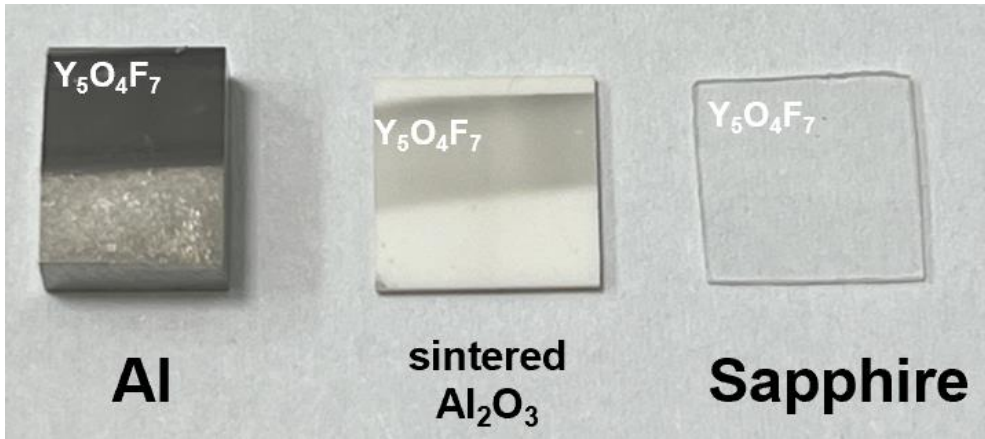


**Figure 4.3.**  $Y_5O_4F_7$  coatings on Al, sintered  $Al_2O_3$ , and C-plane sapphire substrates.

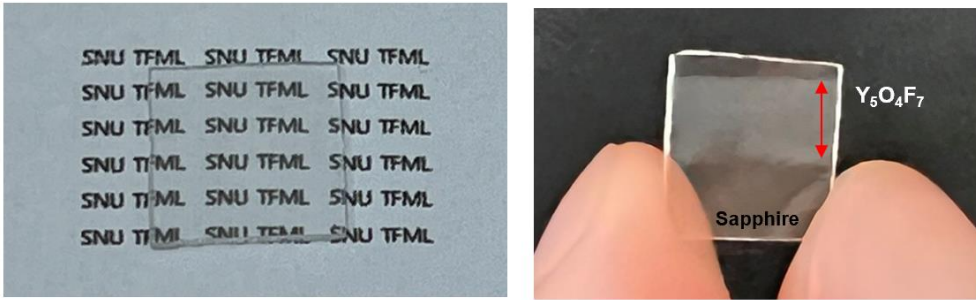


**Figure 4.4.** Transparent  $Y_5O_4F_7$  coating on Sapphire substrate.

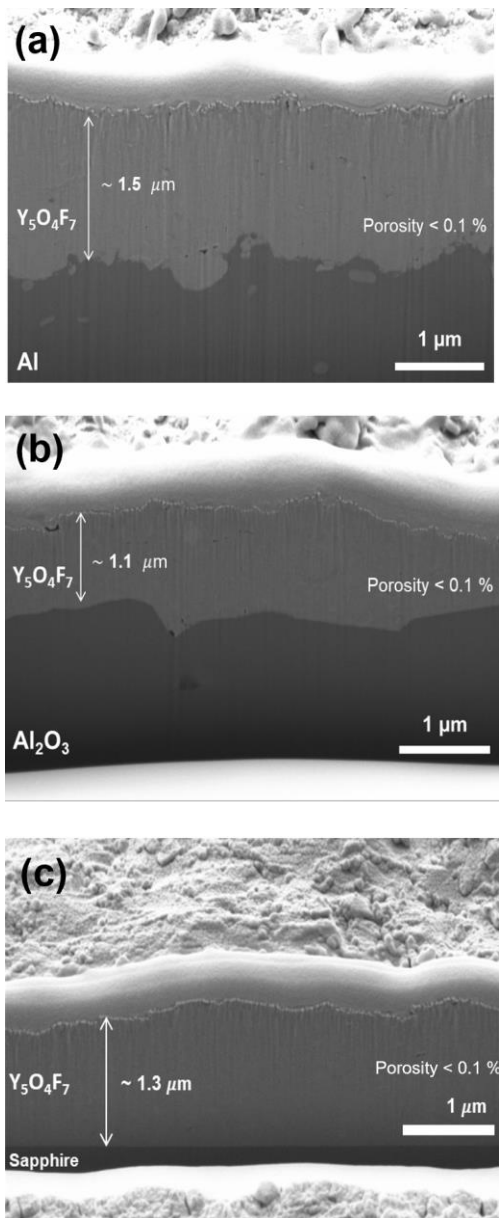


**Figure 4.5.** Cross-section FESEM image of  $Y_5O_4F_7$  coating on (a) Al, (b)  $Al_2O_3$ , and (c) sapphire substrates

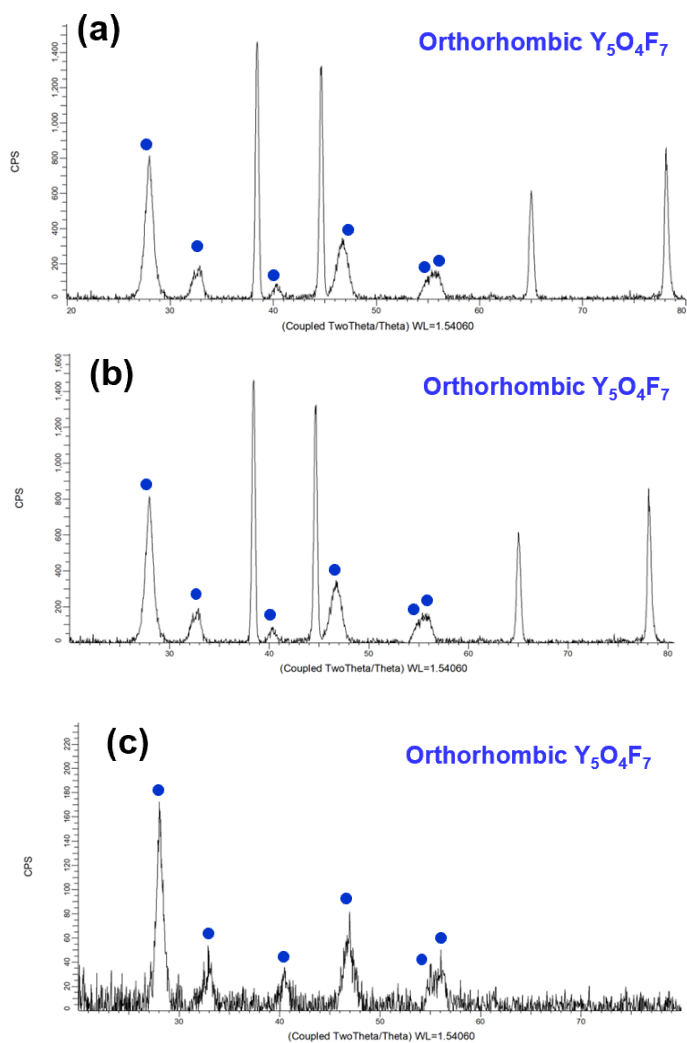


**Figure 4.6.** XRD patterns of  $Y_5O_4F_7$  coating on (a) Al, (b)  $Al_2O_3$ , and (c) sapphire substrates

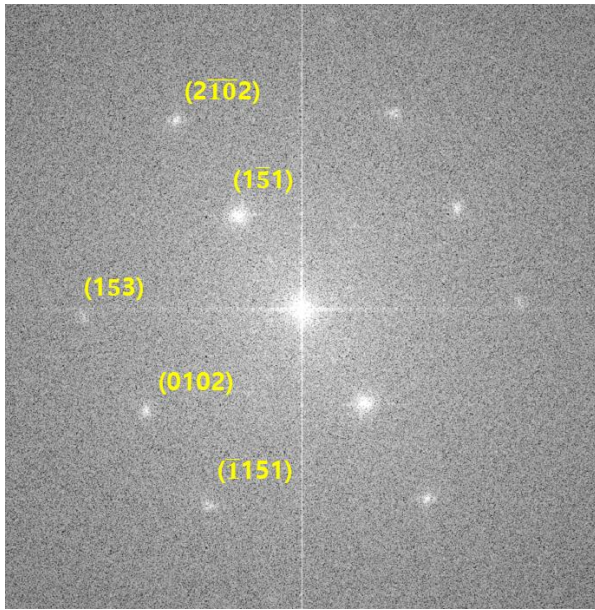


**Figure 4.7.** FFT analysis of  $Y_5O_4F_7$  coating

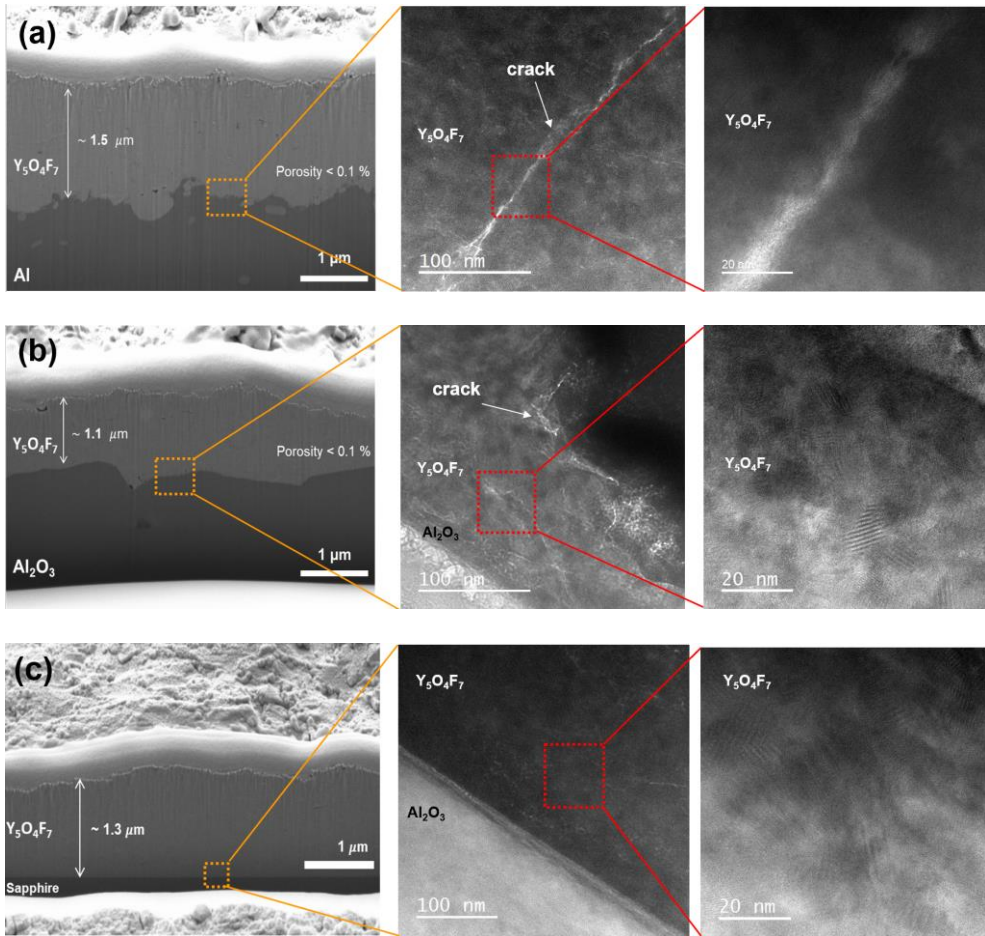


**Figure 4.8.** TEM image of  $\text{Y}_5\text{O}_4\text{F}_7$  coating on (a) Al, (b)  $\text{Al}_2\text{O}_3$ , and (c) sapphire substrates

## Bibliography

- [1] S.-H. Lim and K.-H. Park, An Efficient NAND Flash File System for Flash Memory Storage, *IEEE Trans. Comput.*, 2006, 55(7), p 906–912.
- [2]. S. Hou, W.C. Chen, C. Hu, C. Chiu, K. Ting, T. Lin, W. Wei, W. Chiou, V.J. Lin, and V.C. Chang, Wafer–Level Integration of an Advanced Logic–Memory System Through the Second–Generation CoWoS Technology, *IEEE Trans. Electron Devices*, 2017, 64(10), p 4071–4077.
- [3]. M. Doemling, N. Rueger, G. Oehrlein, and J. Cook, Photoresist Erosion Studied in an Inductively Coupled Plasma Reactor Employing CHF<sub>3</sub>, *J. Vac. Sci. Technol. B: Microelectron. Nanometer Struct. Process. Meas. Phenom.*, 1998, 16(4), p 1998– 2005.
- [4]. D.-M. Kim, Y.-S. Oh, S. Kim, H.-T. Kim, D.-S. Lim, and S.-M. Lee, The Erosion Behaviors of Y<sub>2</sub>O<sub>3</sub> and YF<sub>3</sub> Coatings Under Fluorocarbon Plasma, *Thin Solid Films*, 2011, 519(20), p 6698– 6702.
- [5]. Y. Kim, S. Lee, Y. Cho, S. Kim, and H. Chae, Plasma Atomic Layer Etching of SiO<sub>2</sub> and Si<sub>3</sub>N<sub>4</sub> with Heptafluoropropyl Methyl Ether (C<sub>3</sub>F<sub>7</sub>OCH<sub>3</sub>), *J. Vac. Sci. Technol. A Vac. Surf. Films*, 2020, 38(2), p 022606
- [6]. S.-J. Kim, J.-K. Lee, Y.-S. Oh, S. Kim, and S.-M. Lee, Effect of Processing Parameters and Powder Size on Microstructures and Mechanical Properties of Y<sub>2</sub>O<sub>3</sub> Coatings Fabricated by Suspension Plasma Spray, *J. Korean Ceram.*

Soc., 2015, 52(6), p 395– 402.

[7]. S. Lee, J. Lee, W. Kim, and N.–M. Hwang, Plasma Etching Behavior of YOF Coating Deposited by Suspension Plasma Spraying in Inductively Coupled CHF<sub>3</sub>/Ar Plasma, *Coatings*, 2020, 10(11), p 1023.

[8]. J. Lee, S. Lee, H.N. Han, W. Kim, and N.–M. Hwang, Yttrium Oxyfluoride Coatings Deposited by Suspension Plasma Spraying Using Coaxial Feeding, *Coatings*, 2020, 10(5), p 481.

[9]. A. Joulia, G. Bolelli, E. Gualtieri, L. Lusvarghi, S. Valeri, M. Vardelle, S. Rossignol, and A. Vardelle, Comparing the Deposition Mechanisms in Suspension Plasma Spray (SPS) and Solution Precursor Plasma Spray (SPPS) Deposition of YttriaStabilised Zirconia (YSZ), *J. Eur. Ceram. Soc.*, 2014, 34(15), p 3925–3940.

[10]. J.L. Marque's, G. Forster, and J. Schein, Multi–electrode Plasma Torches: Motivation for Development and Current state–of–theArt, *Open Plasma Phys. J.*, 2009, 2(1), p 89–98.

[11]. J. Kitamura, K. Sato, Z.T. Gifu, and A. Burgess, Crystal and microstructures of plasma sprayed yttrium oxide coatings by axial injection of fine powder slurries, in *Proceedings of the International Thermal Spray Conference*, 2010, p 567–572

[12]. D. Hanft, J. Exner, M. Schubert, T. Stöcker, P. Fuierer, R. Moos An overview of the aerosol deposition method: Process fundamentals and new trends in materials applications *J. Ceram. Sci. Technol*, 6 (2015), pp. 147–182

- [13]. J.J. Choi, J.H. Lee, D.S. Park, B.D. Hahn, W.H. Yoon, H.T. Lin, Oxidation resistance coating of LSM and LSCF on SOFC metallic interconnects by the aerosol deposition process *J. Am. Ceram. Soc.*, 90 (2007), pp. 1926–1929
- [14]. B.-D. Hahn, D.-S. Park, J.-J. Choi, J. Ryu, W.-H. Yoon, J.-H. Choi, J.-W. Kim, Y.-L. Cho, C. Park, H.-E. Kim, Preparation and in vitro characterization of aerosol-deposited hydroxyapatite coatings with different surface roughnesses *Appl. Surf. Sci.*, 257 (2011), pp. 7792–7799
- [15]. S.W. Kim, D.S. Seo, J.K. Lee, Fabrication of xenogeneic bone-derived hydroxyapatite thin film by aerosol deposition method, *Appl. Surf. Sci.*, 255 (2008), pp. 388–390
- [16]. S.H. Cho, Y.J. Yoon, Multi-layer TiO<sub>2</sub> films prepared by aerosol deposition method for dye-sensitized solar cells *Thin Solid Films*, 547 (2013), pp. 91–94
- [17]. S. Baba, J. Akedo Fiber laser annealing of nanocrystalline PZT thick film prepared by aerosol deposition *Appl. Surf. Sci.*, 255 (2009), pp. 9791–9795
- [18]. J. Akedo, Room temperature impact consolidation (RTIC) of fine ceramic powder by aerosol deposition method and applications to microdevices, *J. Therm. Spray Technol.*, 17 (2008), pp. 181–198
- [19]. M.-Y. Cho, D.-W. Lee, P.-J. Ko, S.-M. Koo, J. Kim, Y.-K. Choi, J.-M. Oh, Adhesive Mechanism of Al<sub>2</sub>O<sub>3</sub>/Cu Composite Film via Aerosol Deposition Process for Application of Film Resistor *Electron. Mater. Lett.*, 15 (2019),

pp. 227–237

[20]. D.-W. Lee, O.-Y. Kwon, W.-J. Cho, J.-K. Song, Y.-N. Kim, Characteristics and mechanism of Cu films fabricated at room temperature by aerosol deposition, *Nanoscale Res. Lett.*, 11 (2016), pp. 1–8

[21]. Y.-H. Kim, J.-W. Lee, H.-J. Kim, Y.-H. Yun, S.-M. Nam Silver metallization for microwave device using aerosol deposition *Ceram. Int.*, 38 (2012), pp. S201–S204

[22]. J. Akedo, Aerosol deposition of ceramic thick films at room temperature: densification mechanism of ceramic layers *J. Am. Ceram. Soc.*, 89 (6) (2006), pp. 1834–1839

[23]. S. Amin, H. Panchal, A review on thermal spray coating processes, *transfer*, 2 (2016).

[24]. A. Moridi, S.M. Hassani–Gangaraj, M. Guagliano, M. Dao Cold spray coating: review of material systems and future perspectives, *Surf. Eng.*, 30 (2014), pp. 369–395

[25]. D.W. Lee, H.J. Kim, Y.H. Kim, Y.H. Yun, S.M. Nam Growth process of  $\alpha$ -Al<sub>2</sub>O<sub>3</sub> ceramic films on metal substrates fabricated at room temperature by aerosol deposition *J. Am. Ceram. Soc.*, 94 (2011), pp. 3131–3138

[26]. H. Jami, A. Jabbarzadeh Molecular simulation of high-velocity deposition of titanium dioxide nanoparticles on titanium *Appl. Surf. Sci.*, 542 (2021), Article 148567

- [27]. H. Jami, A. Jabbarzadeh, Ultrafast thermomechanical effects in aerosol deposition of hydroxyapatite nanoparticles on a titanium substrate *Surf. Coat. Technol.*, 382 (2020), Article 125173
- [28]. G. Song, H. Yang, C.J. Hogan Jr, Thermal energy evolution and mechanical deformation of monocrystalline yttria–stabilized zirconia nanoparticles in aerosol deposition processes, *Appl. Surf. Sci.*, 585 (2022), Article 152603
- [29]. D.–M. Chun, S.–H. Ahn, Deposition mechanism of dry sprayed ceramic particles at room temperature using a nano–particle deposition system, *Acta Mater.*, 59 (2011), pp. 2693–2703
- [30]. Tsunoura, T.; Yoshida, K.; Yano, T.; Kishi, Y. Fabrication, characterization, and fluorine–plasma exposure behavior of dense yttrium oxyfluoride ceramics. *Jpn. J. Appl. Phys.* 2017, 56, 06HC02.
- [31]. Shiba, Y.; Teramoto, A.; Goto, T.; Kishi, Y.; Shirai, Y.; Sugawa, S. Stable yttrium oxyfluoride used in plasma process chamber. *J. Vac. Sci. Technol. A Vac. Surf. Films* 2017, 35, 021405.
- [32]. Lin, T.–K.; Wu, D.–S.; Huang, S.–Y.; Wang, W.–K. Preparation, and characterization of sprayed–yttrium oxyfluoride corrosion protective coating for plasma process chambers. *Coatings* 2018, 8, 373.
- [33]. Kim, S.–J.; Lee, J.–K.; Oh, Y.–S.; Kim, S.; Lee, S.–M. Effect of Processing Parameters and Powder Size on

Microstructures and Mechanical Properties of Y<sub>2</sub>O<sub>3</sub> Coatings Fabricated by Suspension Plasma Spray. *J. Korean Ceram. Soc.* 2015, 52, 395.

[34]. Joulia, A.; Bolelli, G.; Gualtieri, E.; Lusvarghi, L.; Valeri, S.; Vardelle, M.; Rossignol, S.; Vardelle, A. Comparing the deposition mechanisms in suspension plasma spray (SPS) and solution precursor plasma spray (SPPS) deposition of yttria-stabilised zirconia (YSZ). *J. Eur. Ceram. Soc.* 2014, 34, 3925–3940.

[35]. Fauchais, P.; Rat, V.; Coudert, J.-F.; Etchart-Salas, R.; Montavon, G. Operating parameters for suspension and solution plasma-spray coatings. *Surf. Coat. Technol.* 2008, 202, 4309–4317.

[36]. Kozerski, S.; Łatka, L.; Pawlowski, L.; Cernuschi, F.; Petit, F.; Pierlot, C.; Podlesak, H.; Laval, J.P. Preliminary study on suspension plasma sprayed ZrO<sub>2</sub>+ 8 wt.% Y<sub>2</sub>O<sub>3</sub> coatings. *J. Eur. Ceram. Soc.* 2011, 31, 2089–2098.

[37]. Kitamura, J.; Sato, K.; Gifu, Z.T.; Burgess, A. Crystal and Microstructures of Plasma Sprayed Yttrium Oxide Coatings by Axial Injection of Fine Powder Slurries. In *Proceedings of the International Thermal Spray Conference*, Beijing, China, 14–16 May 2007; pp. 567–572.

[38]. S.-H. Lim and K.-H. Park, An Efficient NAND Flash File System for Flash Memory Storage, *IEEE Trans. Comput.*, 2006, 55(7), p 906–912.

[39]. S. Hou, W.C. Chen, C. Hu, C. Chiu, K. Ting, T. Lin, W. Wei, W. Chiou, V.J. Lin, and V.C. Chang, Wafer-Level Integration of an Advanced Logic-Memory System Through the Second-Generation CoWoS Technology, *IEEE Trans. Electron Devices*, 2017, 64(10), p 4071-4077.

[40]. M. Doemling, N. Rueger, G. Oehrlein, and J. Cook, Photoresist Erosion Studied in an Inductively Coupled Plasma Reactor Employing CHF<sub>3</sub>, *J. Vac. Sci. Technol. B: Microelectron. Nanometer Struct. Process. Meas. Phenom.*, 1998, 16(4), p 1998-2005.

[41]. D.-M. Kim, Y.-S. Oh, S. Kim, H.-T. Kim, D.-S. Lim, and S.-M. Lee, The Erosion Behaviors of Y<sub>2</sub>O<sub>3</sub> and YF<sub>3</sub> Coatings Under Fluorocarbon Plasma, *Thin Solid Films*, 2011, 519(20), p 6698-6702.

[42]. Y. Kim, S. Lee, Y. Cho, S. Kim, and H. Chae, Plasma Atomic Layer Etching of SiO<sub>2</sub> and Si<sub>3</sub>N<sub>4</sub> with Heptafluoropropyl Methyl Ether (C<sub>3</sub>F<sub>7</sub>OCH<sub>3</sub>), *J. Vac. Sci. Technol. A Vac. Surf. Films*, 2020, 38(2), p 022606.

[43]. S.-J. Kim, J.-K. Lee, Y.-S. Oh, S. Kim, and S.-M. Lee, Effect of Processing Parameters and Powder Size on Microstructures and Mechanical Properties of Y<sub>2</sub>O<sub>3</sub> Coatings Fabricated by Suspension Plasma Spray, *J. Korean Ceram. Soc.*, 2015, 52(6), p 395-402.

[44]. S. Lee, J. Lee, W. Kim, and N.-M. Hwang, Plasma Etching Behavior of YOF Coating Deposited by Suspension Plasma Spraying in Inductively Coupled CHF<sub>3</sub>/Ar Plasma,

[45]. J. Lee, S. Lee, H.N. Han, W. Kim, and N.-M. Hwang, Yttrium Oxyfluoride Coatings Deposited by Suspension Plasma Spraying Using Coaxial Feeding, *Coatings*, 2020, 10(5), p 481.

[46]. A. Joulia, G. Bolelli, E. Gualtieri, L. Lusvarghi, S. Valeri, M. Vardelle, S. Rossignol, and A. Vardelle, Comparing the Deposition Mechanisms in Suspension Plasma Spray (SPS) and Solution Precursor Plasma Spray (SPPS) Deposition of Ytria-Stabilised Zirconia (YSZ), *J. Eur. Ceram. Soc.*, 2014, 34(15), p 3925–3940.

[47]. J.L. Marqués, G. Forster, and J. Schein, Multi-electrode Plasma Torches: Motivation for Development and Current state-of-the-Art, *Open Plasma Phys. J.*, 2009, 2(1), p 89–98.

[48]. J. Kitamura, K. Sato, Z.T. Gifu, and A. Burgess, Crystal and microstructures of plasma sprayed yttrium oxide coatings by axial injection of fine powder slurries, in *Proceedings of the International Thermal Spray Conference*, 2010, p 567–572

[49]. S. Lee, J. Lee, and N. Hwang, Effect of the Dispersion State in Y5O4F7 Suspension on YOF Coating Deposited by Suspension Plasma Spray, *Coatings*, 2021, 11(7), p 831.

[50]. Y. Shiba, A. Teramoto, T. Goto, Y. Kishi, Y. Shirai, and S. Sugawa, Stable Yttrium Oxyfluoride Used in Plasma Process Chamber, *J. Vac. Sci. Technol. A Vac. Surf. Films*, 2017, 35(2), p 021405.

[51]. D.-M. Kim, M.-R. Jang, Y.-S. Oh, S. Kim, S.-M. Lee, and S.-H. Lee, Relative Sputtering Rates of Oxides and Fluorides of Aluminum and Yttrium, *Surf. Coat. Technol.*, 2017, 309, p 694–697.

[52]. Axial III Core Technology, <https://www.mettech.com/coating-technology/axial-III-core-technology.php>. Accessed 2 Dec 2020

[53]. C.T. Rueden, J. Schindelin, M.C. Hiner, B.E. DeZonia, A.E. Walter, E.T. Arena, and K.W. Eliceiri, Image J2: ImageJ for the Next Generation of Scientific Image Data, *BMC Bioinform.*, 2017, 18(1), p 1–26.

[54]. H. Eloussifi, J. Farjas, P. Roura, S. Ricart, T. Puig, X. Obradors, and M. Dammak, Thermoanalytical Study of the Decomposition of Yttrium Trifluoroacetate Thin Films, *Thin Solid Films*, 2013, 545, p 200–204.

[55]. P. Fauchais, A. Joulia, S. Goutier, C. Chazelas, M. Vardelle, A. Vardelle, and S. Rossignol, Suspension and Solution Plasma Spraying, *J. Phys. D Appl. Phys.*, 2013, 46(22), p 224015.

[56]. H. Eloussifi, J. Farjas, P. Roura, J. Camps, M. Dammak, S. Ricart, T. Puig, and X. Obradors, Evolution of Yttrium Trifluoroacetate During Thermal Decomposition, *J. Therm. Anal. Calorim.*, 2012, 108(2), p 589–596.

[57]. R. Tahara, T. Tsunoura, K. Yoshida, T. Yano, and Y.

Kishi, Fabrication of dense yttrium oxyfluoride ceramics by hot pressing and their mechanical, thermal, and electrical properties, *Jpn. J. Appl. Phys.*, 2018, 57(S2), p 06JF04.

[58]. Schaepkens, M.; Bosch, R.; Standaert, T.; Oehrlein, G.; Cook, J. Influence of reactor wall conditions on etch processes in inductively coupled fluorocarbon plasmas. *J. Vac. Sci. Technol. A Vac. Surf. Films* 1998, 16, 2099–2107.

[59]. Ito, N.; Moriya, T.; Uesugi, F.; Matsumoto, M.; Liu, S.; Kitayama, Y. Reduction of particle contamination in plasma-etching equipment by dehydration of chamber wall. *Jpn. J. Appl. Phys.* 2008, 47, 3630.

[60]. May, G.S.; Spanos, C.J. *Fundamentals of Semiconductor Manufacturing and Process Control*; Wiley Online Library: Hoboken, NJ, USA, 2006.

[61]. Tsunoura, T.; Yoshida, K.; Yano, T.; Kishi, Y. Fabrication, characterization, and fluorine-plasma exposure behavior of dense yttrium oxyfluoride ceramics. *Jpn. J. Appl. Phys.* 2017, 56, 06HC02.

[62]. Shiba, Y.; Teramoto, A.; Goto, T.; Kishi, Y.; Shirai, Y.; Sugawa, S. Stable yttrium oxyfluoride used in plasma process chamber. *J. Vac. Sci. Technol. A Vac. Surf. Films* 2017, 35, 021405.

[63]. Kitamura, J.; Tang, Z.; Mizuno, H.; Sato, K.; Burgess, A. Structural, mechanical and erosion properties of yttrium oxide coatings by axial suspension plasma spraying for electronics applications. *J. Therm. Spray Technol.* 2011, 20, 170–185.

[64]. Hou, S.Y.; Chen, W.C.; Hu, C.; Chiu, C.; Ting, K.C.; Lin, T.S.; Wei, W.H.; Chiou, W.C.; Lin, V.J.C.; Chang, V.C.Y.; et al. Wafer-Level Integration of an Advanced Logic-Memory System Through the Second-Generation CoWoS Technology. *IEEE Trans. Electron Dev.* 2017, 64, 4071–4077.

[65]. Blain, M.; Tipton, G.; Holber, W.; Selwyn, G.; Westerfield, P.; Maxwell, K. Particle behaviour in an electron cyclotron resonance plasma etch tool. *Plasma Sour. Sci. Technol.* 1994, 3, 325.

[66]. Fukumoto, H.; Fujikake, I.; Takao, Y.; Eriguchi, K.; Ono, K. Plasma chemical behaviour of reactants and reaction products during inductively coupled CF<sub>4</sub> plasma etching of SiO<sub>2</sub>. *Plasma Sour. Sci. Technol* 2009, 18, 045027.

[67]. Tezani, L.; Pessoa, R.; Maciel, H.; Petraconi, G. Chemistry studies of SF<sub>6</sub>/CF<sub>4</sub>, SF<sub>6</sub>/O<sub>2</sub> and CF<sub>4</sub>/O<sub>2</sub> gas phase during hollow cathode reactive ion etching plasma. *Vacuum* 2014, 106, 64–68.

[68]. Kim, D.-P.; Yeo, J.-W.; Kim, C.-I. Etching properties of Al<sub>2</sub>O<sub>3</sub> films in inductively coupled plasma. *Thin Solid Films* 2004, 459, 122–126.

[69]. Miwa, K.; Takada, N.; Sasaki, K. Fluorination mechanisms of Al<sub>2</sub>O<sub>3</sub> and Y<sub>2</sub>O<sub>3</sub> surfaces irradiated by high-density CF<sub>4</sub>/O<sub>2</sub> and SF<sub>6</sub>/O<sub>2</sub> plasmas. *J. Vac. Sci. Technol. A Vac. Surf. Films* 2009, 27, 831–835.

[70]. Cao, Y.-C.; Zhao, L.; Luo, J.; Wang, K.; Zhang, B.-P.;

Yokota, H.; Ito, Y.; Li, J.-F. Plasma etching behavior of Y<sub>2</sub>O<sub>3</sub> ceramics: Comparative study with Al<sub>2</sub>O<sub>3</sub>. *Appl. Surf. Sci.* 2016, 366, 304–309.

[71]. Kim, D.-M.; Jang, M.-R.; Oh, Y.-S.; Kim, S.; Lee, S.-M.; Lee, S.-H. Relative sputtering rates of oxides and fluorides of aluminum and yttrium. *Surf. Coat. Technol.* 2017, 309, 694–697.

[72]. Kim, D.-M.; Oh, Y.-S.; Kim, S.; Kim, H.-T.; Lim, D.-S.; Lee, S.-M. The erosion behaviors of Y<sub>2</sub>O<sub>3</sub> and YF<sub>3</sub> coatings under fluorocarbon plasma. *Thin Solid Films* 2011, 519, 6698–6702.

[73]. Lin, T.-K.; Wu, D.-S.; Huang, S.-Y.; Wang, W.-K. Preparation and characterization of sprayed-yttrium oxyfluoride corrosion protective coating for plasma process chambers. *Coatings* 2018, 8, 373.

[74]. Kim, S.-J.; Lee, J.-K.; Oh, Y.-S.; Kim, S.; Lee, S.-M. Effect of Processing Parameters and Powder Size on Microstructures and Mechanical Properties of Y<sub>2</sub>O<sub>3</sub> Coatings Fabricated by Suspension Plasma Spray. *J. Korean Ceram. Soc.* 2015, 52, 395.

[75]. Joulia, A.; Bolelli, G.; Gualtieri, E.; Lusvarghi, L.; Valeri, S.; Vardelle, M.; Rossignol, S.; Vardelle, A. Comparing the deposition mechanisms in suspension plasma spray (SPS) and solution precursor plasma spray (SPPS) deposition of yttria-stabilised zirconia (YSZ). *J. Eur. Ceram. Soc.* 2014, 34, 3925–3940.

[76]. Fauchais, P.; Rat, V.; Coudert, J.-F.; Etchart-Salas, R.; Montavon, G. Operating parameters for suspension and solution plasma-spray coatings. *Surf. Coat. Technol.* 2008, 202, 4309–4317.

[77]. Kozerski, S.; Łatka, L.; Pawlowski, L.; Cernuschi, F.; Petit, F.; Pierlot, C.; Podlesak, H.; Laval, J.P. Preliminary study on suspension plasma sprayed ZrO<sub>2</sub>+ 8 wt.% Y<sub>2</sub>O<sub>3</sub> coatings. *J. Eur. Ceram. Soc.* 2011, 31, 2089–2098.

[78]. Kitamura, J.; Sato, K.; Gifu, Z.T.; Burgess, A. Crystal and Micro Structures of Plasma Sprayed Yttrium Oxide Coatings by Axial Injection of Fine Powder Slurries. In *Proceedings of the International Thermal Spray Conference, Beijing, China, 14–16 May 2007*; pp. 567–572.

[79]. Meillot, E.; Vert, R.; Caruyer, C.; Damiani, D.; Vardelle, M. Manufacturing nanostructured YSZ coatings by suspension plasma spraying (SPS): Effect of injection parameters. *J. Phys. D Appl. Phys.* 2011, 44, 194008.

[80]. Szente, R.N. Electrode Erosion in Plasma Torches. *Plasma Chem. Plasma Process.* 1992, 12, 3.

[81]. Marqués, J.L.; Forster, G.; Schein, J. Multi-electrode plasma torches: Motivation for development and current state-of-the-art. *Open Plasma Phys. J.* 2009, 2, 89–98.

[82]. Curry, N.; VanEvery, K.; Snyder, T.; Susnjar, J.; Bjorklund, S. Performance testing of suspension plasma sprayed thermal barrier coatings produced with varied suspension parameters. *Coatings* 2015, 5, 338–356.

## 초 록

본 학위논문에서는 현탁 플라즈마 분무에 의해 석출된 YOF 코팅의 코팅 거동은 고출력 동축 이송법을 이용하여 조사하였다. YOF 코팅의 증착 속도 및 밀도 모두 플라즈마 출력에 따라 증가하였으며, 이는 Ar/H<sub>2</sub>/N<sub>2</sub>의 가스비와 아크 전류에 의해 결정되었다. 현탁액의 공급속도가 분당 0.045 표준리터(slm)인 20회 스캔에 대해 112, 83, 67, 59 kW의 플라즈마 출력에서 코팅 두께는 각각  $58 \pm 3.4$ ,  $25.8 \pm 2.1$ ,  $5.6 \pm 0.6$ ,  $0.93 \pm 0.4 \mu\text{m}$ 였다. 112, 83 및 67 kW의 해당 플라즈마 출력에서 공극률은  $0.15\% \pm 0.01\%$ ,  $0.25\% \pm 0.01\%$ ,  $5.50\% \pm 0.40\%$ 였다. 고해상도 X선 회절(HR-XRD)은 112 kW에서 증착된 코팅의 주 피크와 부 피크가 각각 trigonal YOF와 cubic Y<sub>2</sub>O<sub>3</sub>에서 기인함을 보여준다. 분무 가스의 유속을 15 slm에서 30 slm으로 증가시키면 YOF 코팅의 공극률은  $0.22\% \pm 0.03\%$ 에서  $0.07\% \pm 0.03\%$ 로 감소하였다. 112 kW에서 증착된 일부 Y<sub>2</sub>O<sub>3</sub>를 포함하는 YOF 코팅의 비커스 경도는  $550 \pm 70 \text{ HV}$ 였다.

상기 현탁액 플라즈마 스프레이(SPS) 공정을 이용하여 이트륨 옥시플루오라이드의 플라즈마 내성 코팅을 개발하기 위하여, 불소가 풍부한 이트륨 옥시플루오라이드 코팅을 위한 혼합 Y<sub>5</sub>O<sub>4</sub>F<sub>7</sub>/YF<sub>3</sub> 현탁액을 개발하였다. 상대적으로 내플라즈마성이 약해 바람직하지 않은 cubic 및 monoclinic Y<sub>2</sub>O<sub>3</sub>는 대기압에서 SPS 공정에 의해 Y<sub>5</sub>O<sub>4</sub>F<sub>7</sub> 현탁액이 증착된 옥시플루오라이드 이트륨 코팅에 함께 형성되었다. Y<sub>2</sub>O<sub>3</sub>의 형성을 최소화하기 위해 대기압에서 SPS 코팅의 메커니즘을 유추하여 제안하고 Y<sub>5</sub>O<sub>4</sub>F<sub>7</sub> 및 YF<sub>3</sub> 입자를 포함하는 질량비가 다른 4개의 현탁액으로 증착된 코팅들을 분석하였다. SPS 공정 중 현탁액 내의 Y<sub>5</sub>O<sub>4</sub>F<sub>7</sub> 입자는 증발 공정 후 남은 열에너지를 이용한 화학반응을 통해 수소와 산소와 반응하여 코팅 표면 근처에 YOF 및 Y<sub>2</sub>O<sub>3</sub> 복합체를 형성하였다. X선 회절(XRD)과 고해상도 3차원 X선 단층 현미경

시스템(HR-XRM)을 사용하여  $Y_5O_4F_7$  현탁액이 증착된 코팅 표면 근처에 비교적 많은 양의  $Y_2O_3$ 가 형성되어 있는 반면,  $Y_2O_3$ 의 형성은 최소화하고 옥시플루오라이드의 형성은 극대화하였다. 혼합  $Y_5O_4F_7/YF_3$  서스펜션으로 7:3의 질량비로 증착된 코팅. 최소량의  $Y_2O_3$ 를 포함하는 이 코팅은 높은 플라즈마 저항을 제공할 것으로 예상된다.

YOF보다 플라즈마 저항성이 우수한  $Y_5O_4F_7$  코팅을 증착하기 위해 에어로졸 증착이 연구되었다. Al, 소결  $Al_2O_3$ , C-평면 사파이어 기판 위에  $Y_5O_4F_7$  코팅을 증착하였으며, XRD 및 SEM 이미지 분석을 통해 세 샘플 모두 SEM 이미지에 조밀한 코팅을 형성함을 확인하였다. 그 중 Al, 소결된  $Al_2O_3$  기재에 증착된 코팅은 검은색인 반면, 사파이어 기재에 증착된 코팅은 투명하였다. TEM 분석 결과, 검은 코팅은 나노크랙이 있는 반면, 투명 코팅은 나노크랙이나 나노기공이 없는 것을 확인할 수 있었다.

**주요어 :** 플라즈마 저항성, 현탁액 플라즈마 분사, 옥시플루오린화이트륨, 에어로졸 증착.

**학 번 :** 2017-24472